SERI/STR--211-3526

DE89 009444

SERI/STR-211-3526
UC Category: 271
DE89009444

Research on High-Efficiency, Multiple-Gap, Multijunction, Amorphous-Silicon-Based Alloy Thin-Film Solar Cells

Semiannual Subcontract Report 1 March 1988 - 31 August 1988

S. Guha, Principal Investigator
Energy Conversion Devices, Inc.
Troy, Michigan

June 1989

SERI Technical Monitor: B. Stafford

Prepared under Subcontract No. ZB-7-06003-4

Solar Energy Research Institute
A Division of Midwest Research Institute

1617 Cole Boulevard
Golden, Colorado 80401-3393

Prepared for the
U.S. Department of Energy
Contract No. DE-AC02-83CH10093

NOTICE

Printed in the United States of America
Available from:
National Technical Information Service
U.S. Department of Commerce
5285 Port Royal Road
Springfield, VA 22161

Price: Microfiche A01
Printed Copy A04

Codes are used for pricing all publications. The code is determined by the number of pages in the publication. Information pertaining to the pricing codes can be found in the current issue of the following publications which are generally available in most libraries: *Energy Research Abstracts (ERA)*; *Government Reports Announcements* and Index (*GRA* and I); *Scientific and Technical Abstract Reports (STAR)*; and publication NTIS-PR-360 available from NTIS at the above address.

PREFACE

This Semi-Annual Report covers the work performed by Energy Conversion Devices, Inc., for the period 1 March 1988 to 31 August 1988 under Sub-Contract number ZB-7-06003-4. The following personnel participated in the research program.

A. Bannerjee, C. Bernotaitis, J. Burdick, E. Chen, T. Glatfelter, S. Guha (Principal Investigator), G. Hammond, M. Hopson, T. Laarman, M. Lycette, R. Mohr, P. Nath, A. Pawlikiewicz, I. Rosenstein, R. Ross, D. Wolf, J. Yang, and K. Younan.

We acknowledge useful discussions with H. Fritzsche, S. J. Hudgens, and S. R. Ovshinsky, and would also like to thank V. Trudeau for preparation of this report.

CONTENTS

SECTION 1
INTRODUCTION

This research program is directed toward the advancement of understanding of amorphous silicon-based alloys and their use in small area multi-junction solar cells. The principal objectives of the program are: i) to develop a broad scientific base for the chemical, structural, optical and electronic properties of amorphous silicon-based alloys; ii) to determine the optimum properties of these alloy materials as they relate to high efficiency cells; iii) to determine the optimum device configuration for multi-junction cells; and iv) to demonstrate by the end of February, 1990 the proof-of-concept multi-junction amorphous silicon alloy-based solar cells having an efficiency of 18% under standard AM1.5 global solar insolation conditions and having an area of at least 1 cm^2.

The program is divided into three sub-tasks. Sub-task 1, materials research, is directed toward preparing and optimizing amorphous silicon (a-Si) alloy-based materials for use in high efficiency multi-junction devices. This sub-task also includes the necessary research to improve the properties of optically-transparent/conducting-oxide contacts and any necessary barrier layers required by the multi-junction cell design. Sub-task 2, single-junction solar cell research, involves the preparation and characterization of single-junction cells (incorporating materials from Sub-task 1) for diagnostic purposes and for use in high efficiency multi-junction cells. Sub-task 3, multi-junction solar cell research, involves fabrication of high efficiency, stable multi-junction solar cells incorporating the materials and the single-junction cells developed, respectively, in Sub-tasks 1 and 2. Sub-tasks 2 and 3 also involve device modeling to guide experiments for optimization of device efficiency.

During Phase I of the program, which ended February, 1988, significant advances were made both in the areas of material development and cell efficiency. In this report we discuss the progress made during the period March-August, 1988. A major focus of the program was in the optimization of a novel multiple-graded structure that enhances cell efficiency through the use of band-gap profiling. In the following sections, we discuss in detail the principle of operation of devices incorporating such structure, computer simulations for the same, and experimental results for both single- and multi-junction cells using the novel structure.

SECTION 2
MATERIALS RESEARCH

2.1. INTRODUCTION

In Phase I of the program, we have reported on the development of both wide band-gap a-Si:C alloys and narrow band-gap a-Si:Ge alloys for use in the multi-gap cells. In this report, we discuss the development of wide gap microcrystalline doped layers which would allow more light to be incident on the intrinsic layer of the cell so as to increase the short-circuit current densities. We also discuss the optimization of chemically deposited and sputtered ZnO layers which are used in conjunction with back reflectors.

2.2. MICROCRYSTALLINE WIDE BAND-GAP DOPED LAYERS

We have previously reported the development of microcrystalline p-type layers. We showed that the microcrystalline materials have higher conductivities and lower absorption loss than the corresponding amorphous materials. Incorporation of these layers in solar cells had given rise to higher open-circuit voltage and short-circuit current. In a triple-cell configuration there are six layers of doped material, and reduction of optical loss in these materials, even by a small amount, would result in an increase in short-circuit current density. Moreover, development of wide band-gap doped layers is expected to cause further enhancement of the open-circuit voltage.

One way of increasing the band-gap of a-Si alloys is to add a band-gap widening element such as C, O or N to the material. Efforts to obtain microcrystalline material incorporating these elements have not been, in general, successful, since it is known that C, N or O inhibit crystallization. There have been recent reports that using microwave glow-discharge in the electron cyclotron resonance regime, it is possible to obtain microcrystalline SiC alloys with an optical gap exceeding 2 eV. Use of this method, however, needs special design of the reaction chamber, power supplies and electrodes. We have developed a technique by which, using a conventional rf glow-discharge technique, it is possible to obtain both n- and p-type microcrystalline material incorporating C or N. A deposition regime was

identified consisting of gas mixtures heavily diluted with hydrogen, high rf power density and a suitable temperature region. Both fluorinated and non-fluorinated materials have been developed.

A typical wide band-gap microcrystalline n-type SiN alloy was characterized by a dark conductivity of 2 $(\Omega\ cm)^{-1}$, an absorption constant at 5000 Å of about $2.5 \times 10^{4}\ cm^{-1}$. The optical band-gap of the material is about 2 eV. Based on transmission electron microscopy and Raman spectroscopy results, crystallite sizes were found to be between 60 to 100 Å with a volume fraction greater than 70%. The crystallites are those of silicon embedded in an a-SiN matrix.

Microcrystalline p-type SiC alloys with an optical gap in the range 2.1 to 2.2 eV were deposited with dark conductivity exceeding 1 $(\Omega\ cm)^{-1}$. The grain size and the volume fraction were similar to those of microcrystalline SiN. Typical carbon content was 5 to 10%. Thin microcrystalline p-type SiC layers were incorporated in single-junction n-i-p cells. The quantum efficiency of one such cell at 400 nm was found to be 66%. The cell had an open-circuit voltage of 0.95V.

2.3. REFLECTION VERSUS ANGLE STUDIES OF BACK REFLECTOR MATERIALS AND STRUCTURES

In order to increase the conversion efficiency of our multi-junction photovoltaic devices, the performance of each layer needs to be optimized. Two key improvements involve increasing the optical absorption in the active regions (the i-layers) and the subsequent increase in the collection of the photogenerated carriers. These aspects of the device can be improved by, among other things, changing the band-gap and/or the thickness of the individual layers. An additional technique used to increase optical absorption and carrier collection (thereby increasing the short-circuit current of the device) involves the improvement of the substrate by the incorporation of a back reflector between the substrate and the a-Si alloy material. This enables light which is only weakly absorbed on an initial pass through the a-Si alloy layers to be reflected back into the device, allowing it to have additional passes through the

active layers and increasing its optical absorption therein. Along these lines, then, we at ECD have a program to study various back reflector materials and structures with the goal of increasing the overall short-circuit current (Jsc) of our solar cells by improving the red-light absorption in the bottom-cell i-layer.

Various types of back reflectors studied in this program include both specular as well as diffuse scatterers. This program involves the deposition of a variety of materials (such as Ag, Al, Ti, ZnO, etc.) on our stainless steel substrates using various combinations of structures and under different deposition conditions (varying such parameters as temperature, pressure, etc.). In addition, it involves measurement and analysis of both the back reflectors themselves, as well as the devices fabricated on top of them. To assist in the study of the back reflector materials, especially those deposited in such a manner as to be diffuse scatterers, a special reflection measurement system was designed and constructed. This system was built to enable measurement of reflection versus angle from -90^{o} to $+90^{o}$. A schematic of the R vs θ measurement system is shown in Fig. 1.

Note from Fig. 1 that we have two parts to the R vs θ apparatus. One part, called the Wide Angle measurement, measures from -90^{o} to $+90^{o}$ but does not measure the center $\pm 18^{o}$ due to the detector blocking the incident light beam. Because of this, a second measurement is performed, obtained by deflecting the reflected light beam off to one side and measuring the Near Normal reflection (-20^{o} to $+20^{o}$). These two R vs θ measurements combined give us information about both the wide angle (diffuse) and near normal (specular) reflective properties of the sample under study.

The first measurements performed using the R vs θ system were of some common substrates and standard samples. Figure 2 shows a specular silver substrate with a large spike at 0^{o}, as expected. Figure 3 shows a perfect Lambertian scatterer made of diffuse opal glass. The observed cosine response of the reflection vs angle is what is expected from a Lambertian surface, and we use this with a silver mirror behind it as our standard R vs θ reference sample.

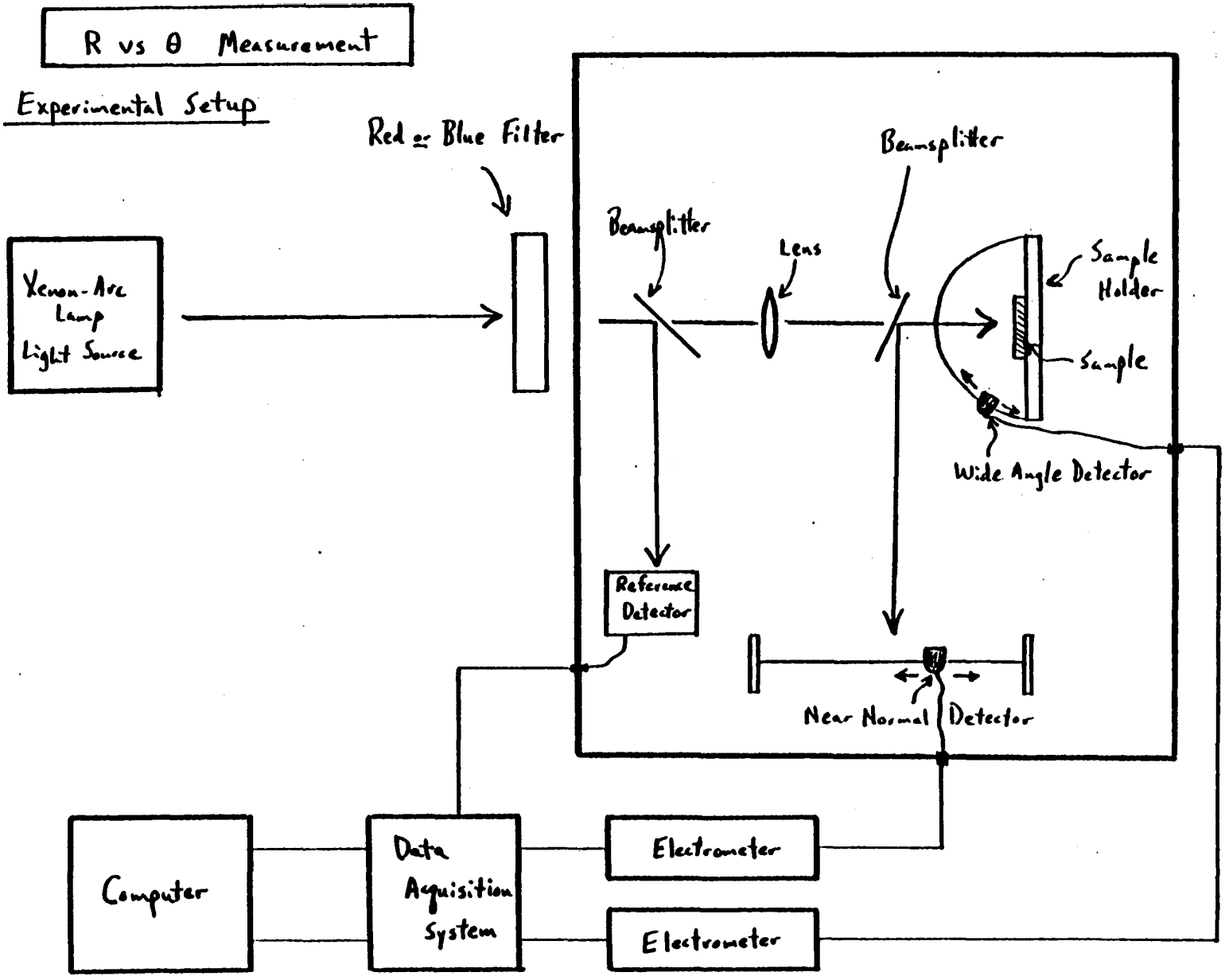

Fig. 1. Schematic of the R vs θ measurement apparatus.

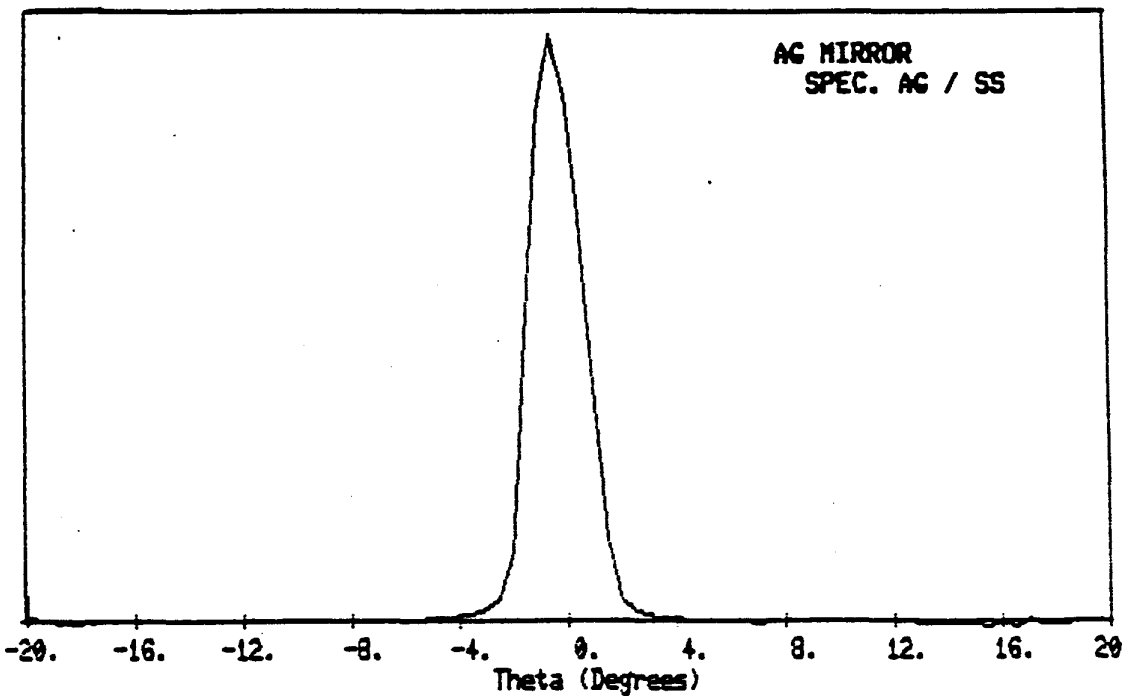

Fig. 2. R vs θ plot of specular silver on a stainless steel substrate.

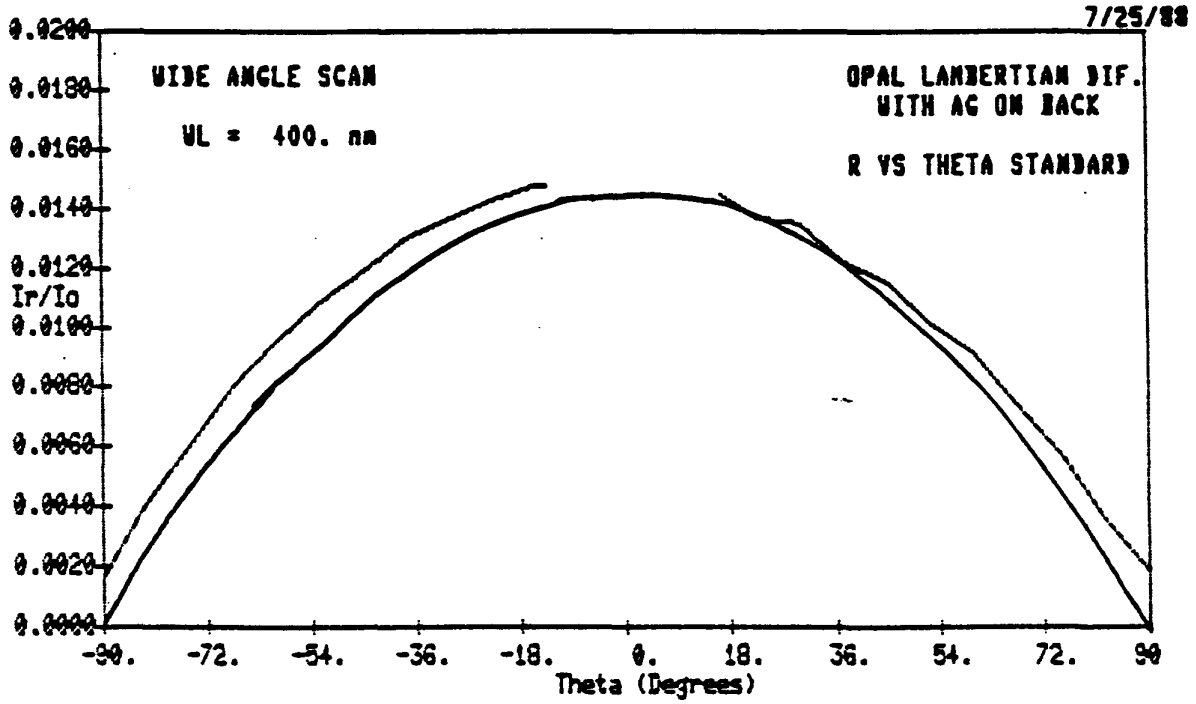

Fig. 3. R vs θ plot of a perfect Lambertian scatterer made from diffuse opal glass.

Other early experiments involved reflection off the front surface of a-Si alloy devices, both from the ITO and from the a-Si alloy material itself. We performed these measurements under both blue and red light. As expected, the ITO reflection was lower in the blue (because of its AR coating properties) than in the red. The reflection from the a-Si alloy material had a larger wide-angle signal from the devices made on diffuse substrates and a larger near-normal signal from the devices made on specular substrates.

Next we looked at different back reflector materials and structures, which had been fabricated under various deposition conditions. It should be noted here that although the wavelength of interest for these substrate reflection studies is in the red, the actual wavelength of the light inside the device is in the blue or UV end of the spectrum. This is because light which is red in air becomes blue inside the a-Si material due to its index of refraction being approximately 3-5. It is this light which is striking the substrate surface. Our measurements were actually performed using 400 nm (blue) light (instead of UV light) to increase our signal-to-noise ratio (since our light source has little flux in the UV portion of the spectrum).

One experiment we performed was a comparison of Al to Ag substrates. Figure 4 (a and b) shows these results. Note that the Al wide angle reflection, although lower than the Ag, has a shape which closely resembles the cosine response of the Lambertian scatterer (Fig. 3). This has led us to study a variety of combinations of Ag and Al as back reflector materials, hopefully gaining from both the high reflectivity of the Ag and the diffuse scattering properties of the Al.

Another study we performed was a combination of two experiments. One was to look at the properties of the back reflector materials versus deposition temperature; the other was to compare the R vs θ results with our quantum efficiency measurement to see if we could get meaningful comparisons between these two measurements. The results are shown in Figs. 5-7. Note that the near normal reflection (b in

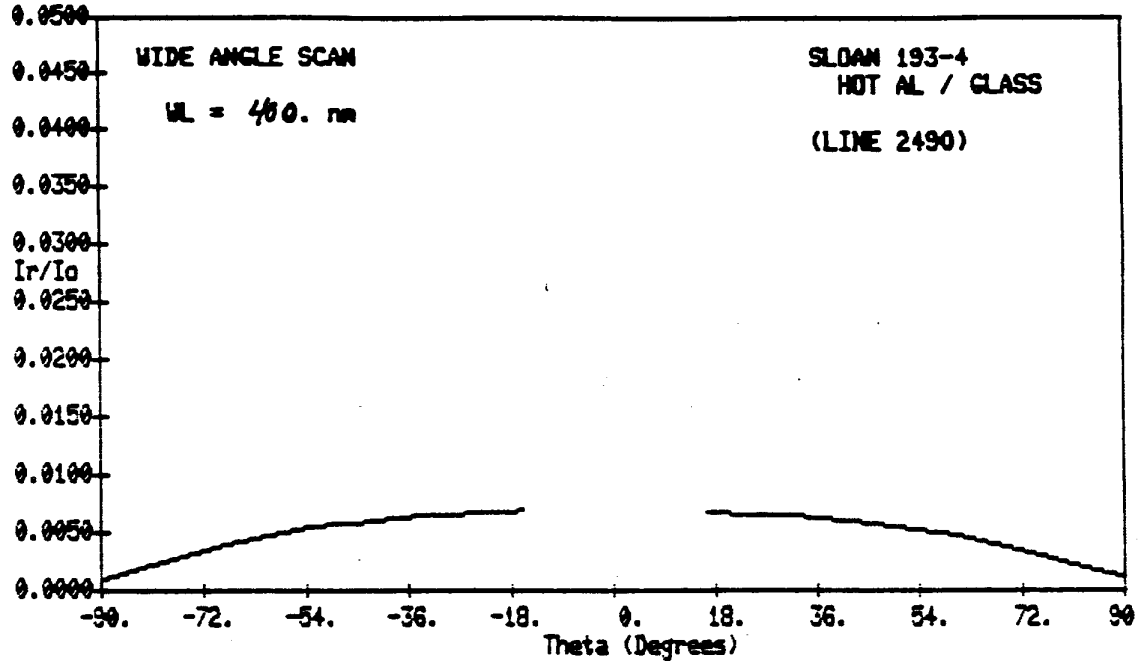

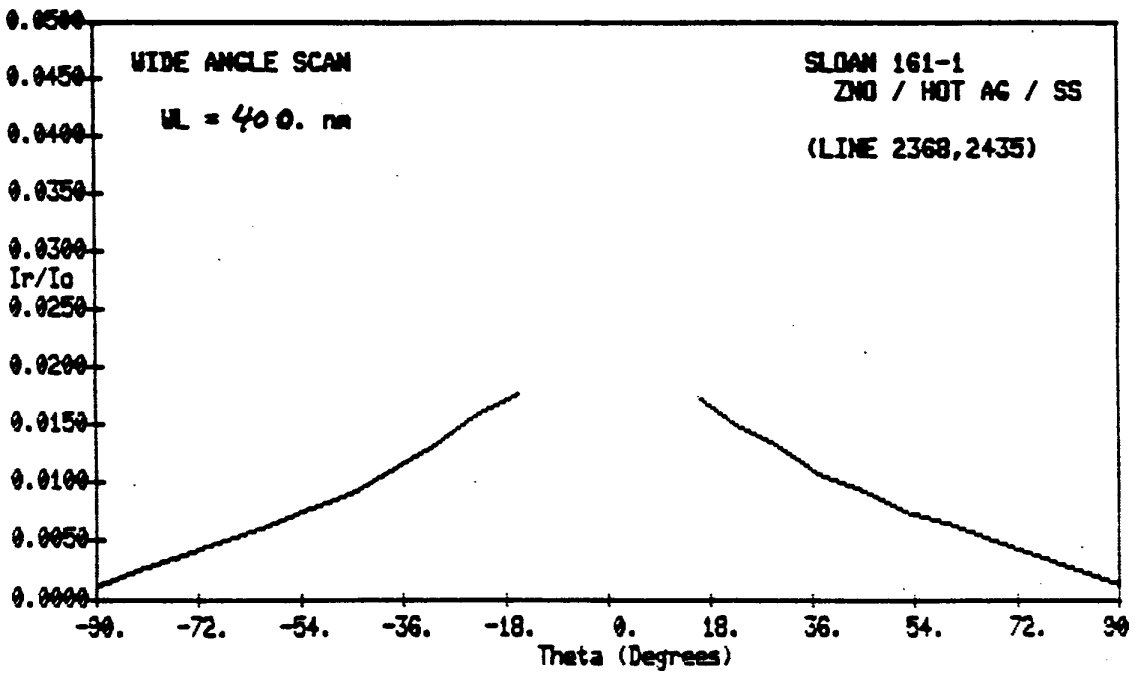

Fig. 4. R vs θ plots of (a) diffuse aluminum and (b) diffuse silver on a stainless steel substrate.

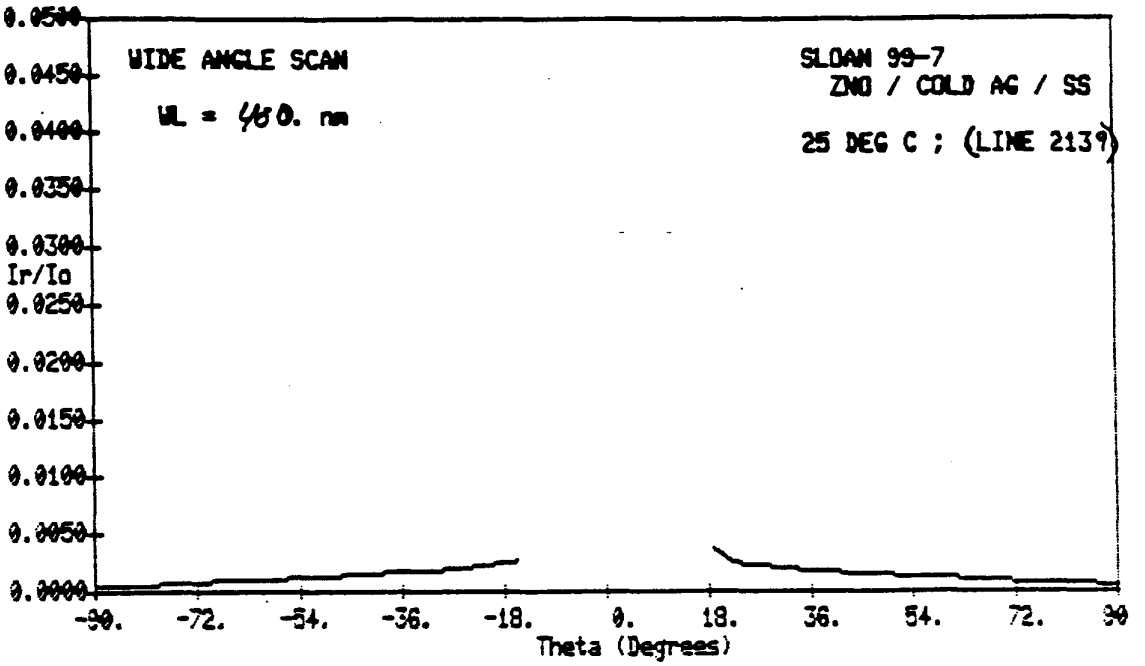

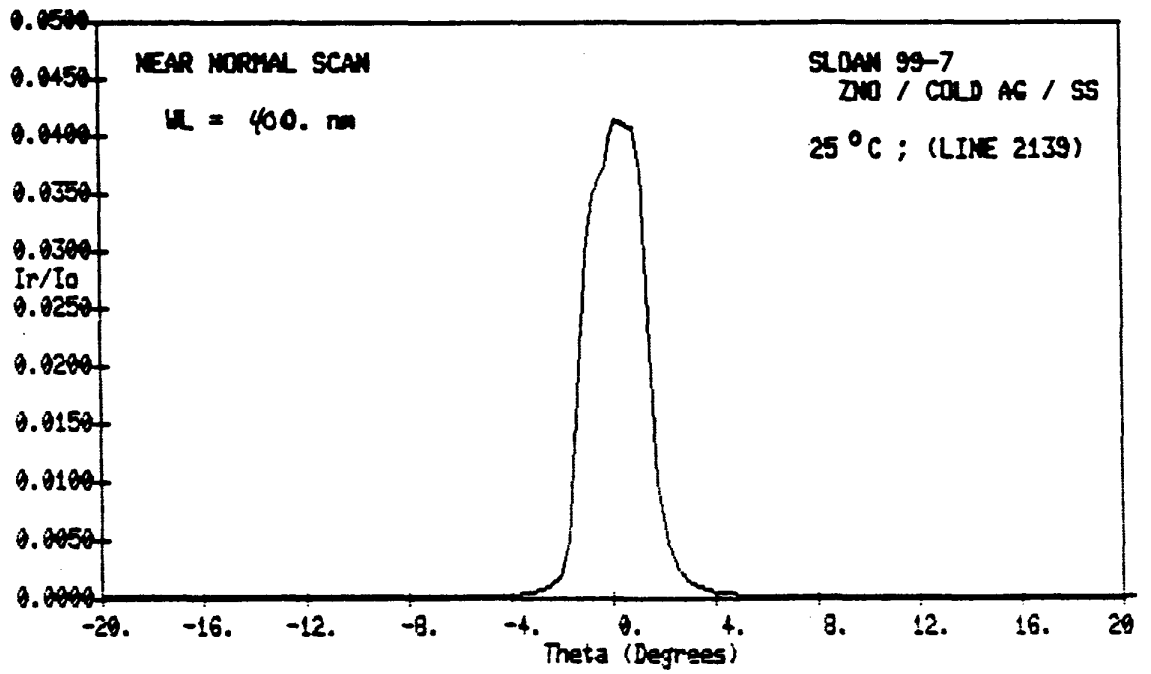

Fig. 5. R vs θ plots of both (a) wide angle reflection and (b) near normal reflection for diffuse Ag deposited on stainless steel at 25°C.

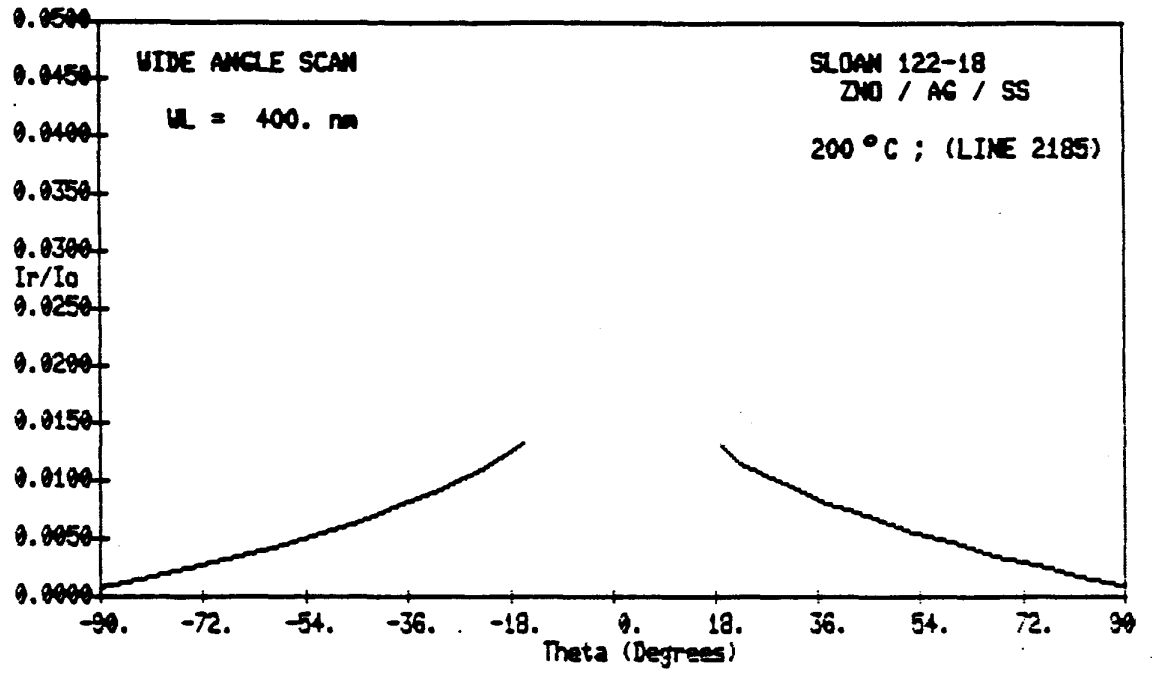

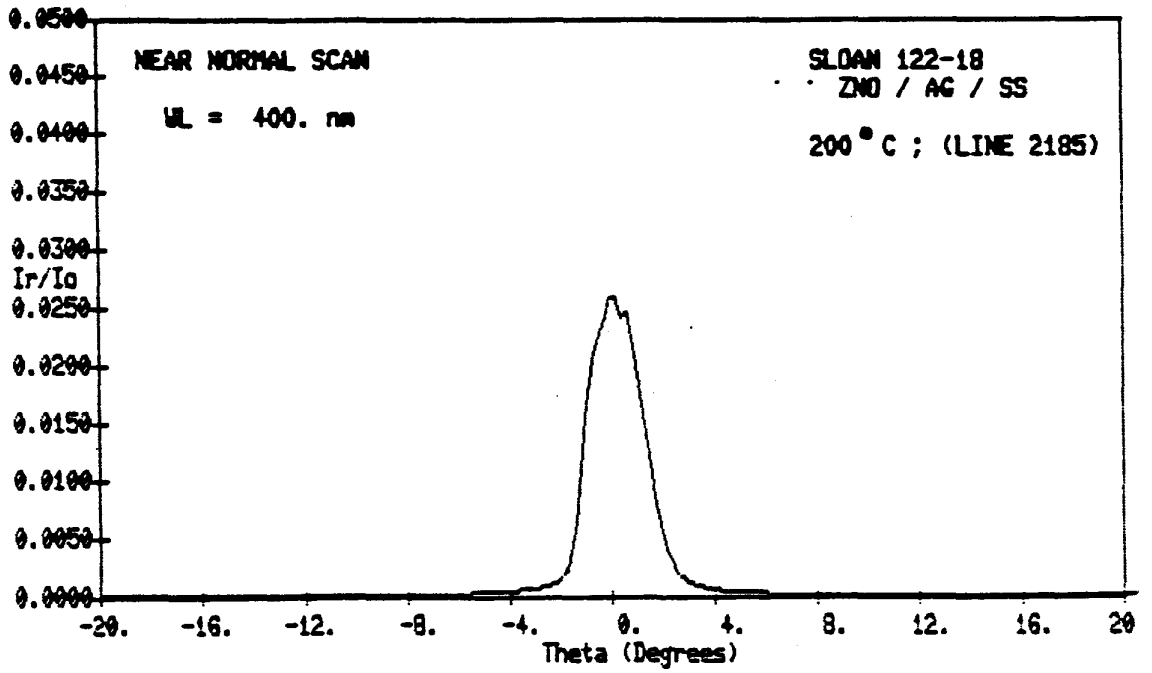

Fig. 6. R vs θ plots of both (a) wide angle reflection and (b) near normal reflection for diffuse Ag deposited on stainless steel at 200°C.

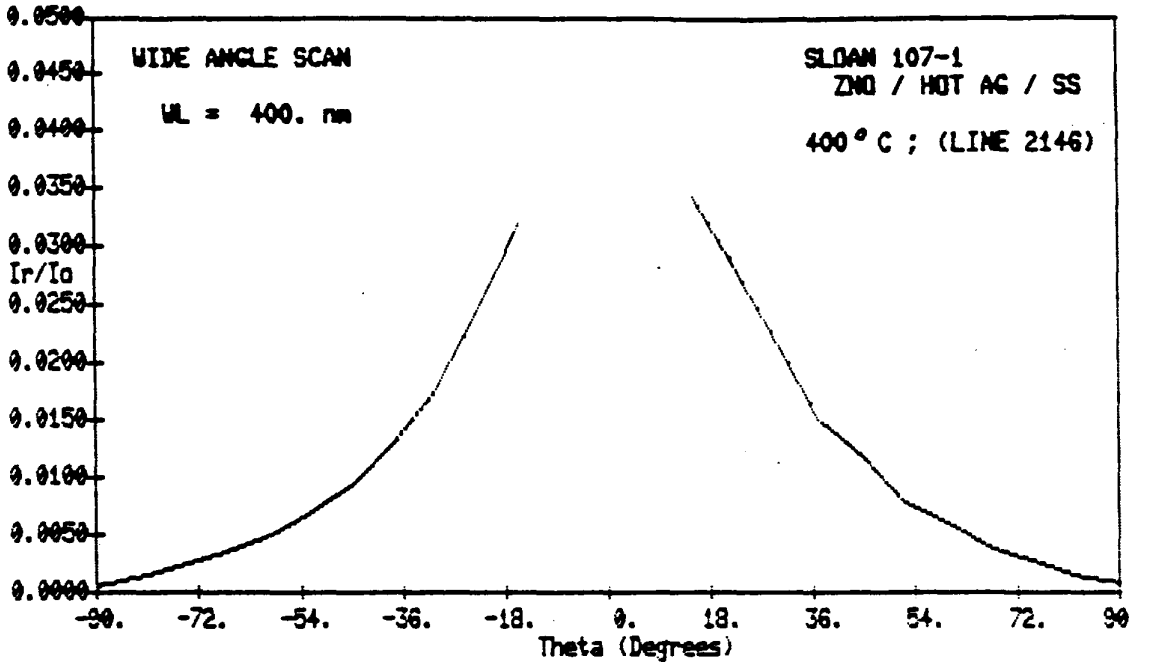

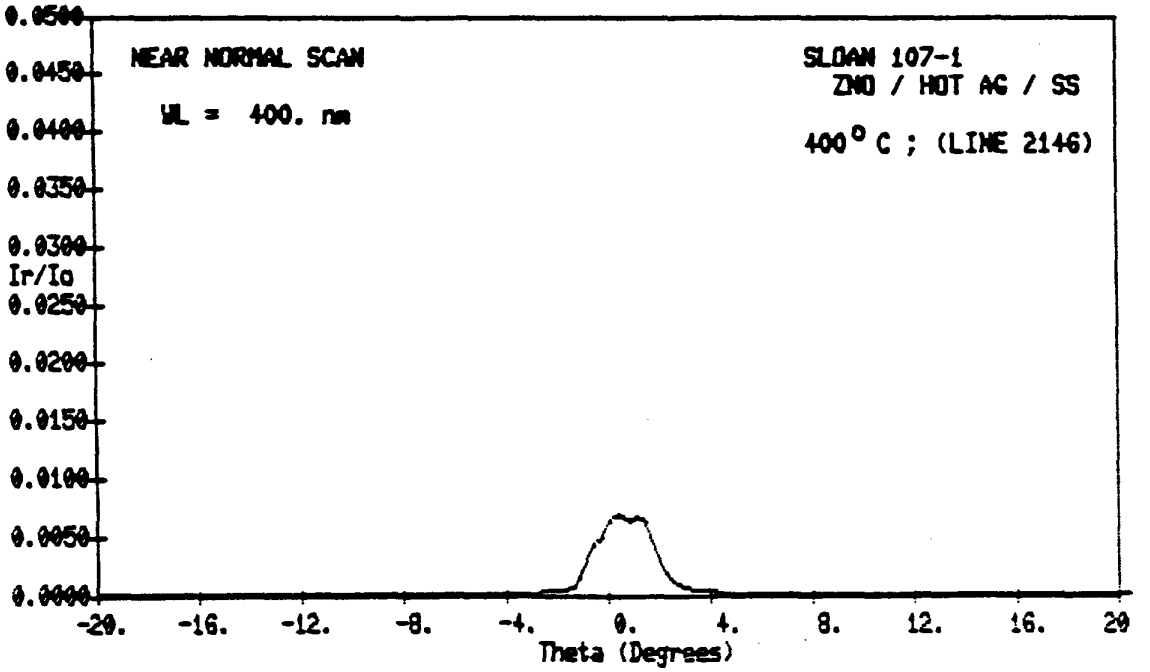

Fig. 7. R vs θ plots of both (a) wide angle reflection and (b) near normal reflection for diffuse Ag deposited on stainless steel at 400°C.

each figure) decreases and the wide angle reflection (a in the figures) increases as we increase the deposition temperature from 25°C to 400°C. Also note a corresponding increase in the device red short-circuit current, obtained by integrating the $Q(\lambda)$ curve from 600-950 nm (see Fig. 8). This last result is important because it points to the correlation between the R vs θ measurement of a substrate (before a device has been made on it) and the $Q(\lambda)$ measurement of a finished solar cell. More studies of this kind will allow further development and improvement of our back reflector materials to further enhance the red-wavelength response and increase our multi-junction device conversion efficiency.

2.4. CHEMICALLY DEPOSITED ZnO FILMS FOR BACK REFLECTOR APPLICATIONS

In the back reflector work discussed in Sec. 2.3., ZnO films were prepared by magnetron sputtering which limits the rate of deposition to $\leq$ 5Å/s for good quality films. This limitation provides a constraint in upscaling the deposition process for incorporation in our roll-to-roll production machine in terms of both physical space and start-up costs.

With the above background, we have explored an alternative technique for the deposition of ZnO films with the following objectives: 1) to increase the deposition rate to $\geq$ 10Å/s without any deleterious effect on the film quality, 2) to cut down the cost of the films per square foot in terms of start-up and deposition operations for production application, and 3) to investigate if a better quality texture can be obtained. The results obtained to date are very encouraging and the project is an ongoing one.

The ZnO film deposition technique is based on a chemical process incorporating inexpensive, readily available, and non-toxic chemicals. The process itself is simple and needs no expensive equipment. The deposition technique is, at present, set up for 3" x 3" substrates. The process is being scaled up to deposit uniform films over 1 sq. ft. The rate of deposition is very high -- typically ~ 20-40Å/s -- with further enhancement expected. The work reported here is on ZnO films deposited at ~ 20Å/s.

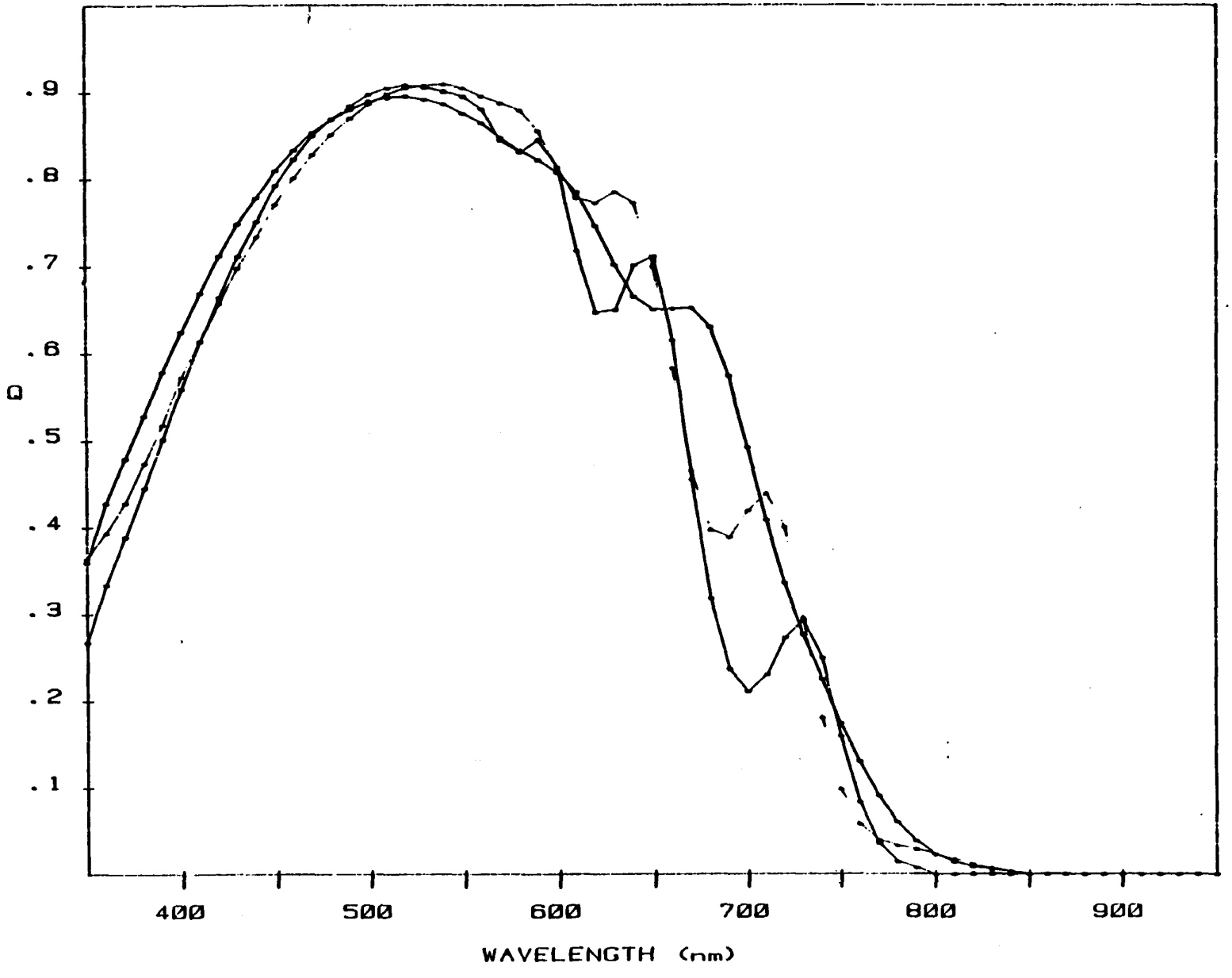

Fig. 8. Quantum efficiency plots of devices made on diffuse Ag/SS back reflectors at 25°C, 200°C, and 400°C. Red Jsc is obtained by integrating the Q(λ) curve from 600 nm to 950 nm.

Two types of ZnO films have been prepared: 1) pure ZnO and 2) In-doped ZnO. The pure ZnO films have higher electrical resistivity (~ $10^3 \Omega$-cm) than the doped films and exhibit photoconductivity. The resistivity under illumination (100mW/cm^2) is ~ 10 ohm-cm. Some properties of the ZnO films are tabulated in Table I. The photoconductivity of the films becomes quenched upon annealing in vacuum. Incorporation of In in the films leads to improved electrical characteristics and quenching of the photoconductivity. The electrical resistivity of ZnO films doped with ~ 4 at.% In is 5×10^{-3} ohm-cm. The films are optically highly transmitting. The transmittance and reflectance characteristics of a 2000Å thick film on glass are shown in Fig. 9. The absorptance in the wavelength range 500-800 nm is < 2%.

Table I. Properties of ZnO films deposited by a chemical process.

Film Type	Undoped ZnO	In Doped (4 at.%) ZnO
ρ_D (Ω cm)	10^3	5×10^{-3}
ρ_L (Ω cm)	5×10^{-3}	5×10^{-3}
Optical Absorptance of 2000Å thick film (%)	< 2%	< 2%

The films exhibit excellent texture as measured by reflected optical dispersion of an incident beam of laser light on the sample. The dispersion characteristics of a pure ZnO film of thickness ~ 3 μm on 1) a glass substrate and 2) a sputtered textured Ag film/stainless steel substrate are shown in Fig. 10. It is noteworthy that the excess specular component of the reflected light (which is the major component for Ag films) is totally absent for the ZnO films. The dispersion properties are dependent on film thickness and deposition temperature.

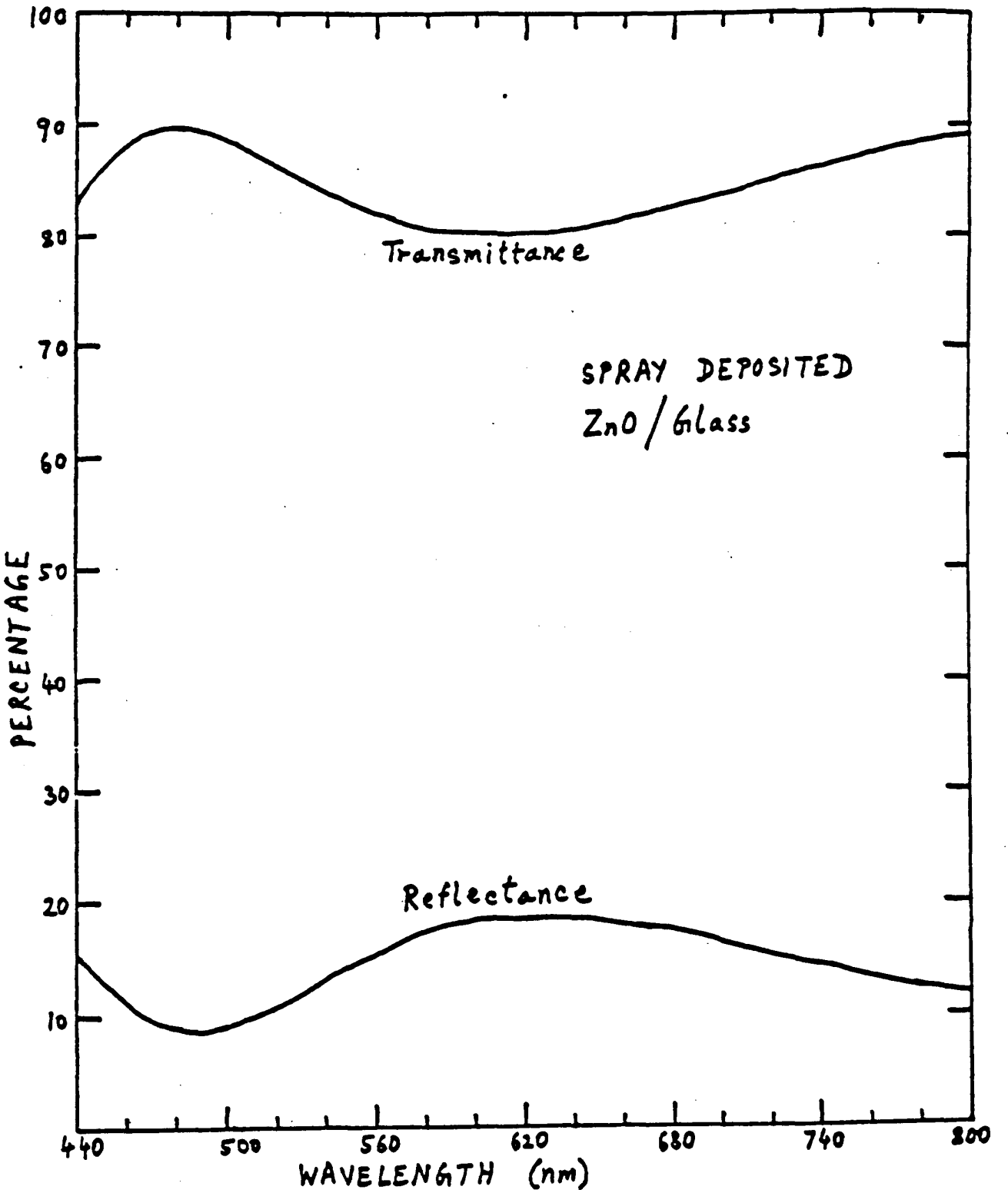

Fig. 9. Transmittance and Reflectance of a 2000Å thick chemically deposited ZnO film on glass substrate as a function of wavelength.

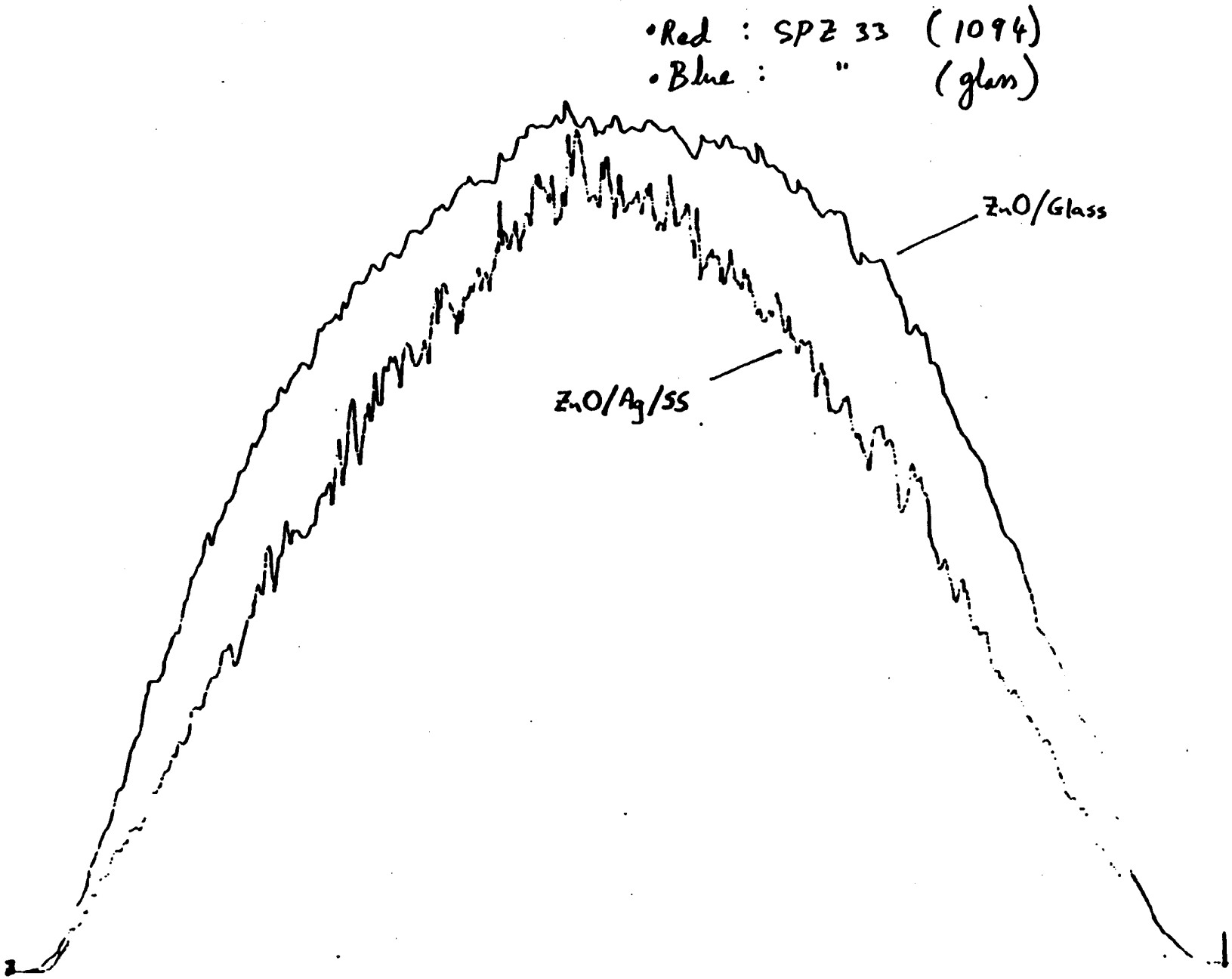

Fig. 10. Optical dispersion characteristics (using an incident laser beam) of a chemically deposited ZnO film on glass and on textured Ag substrates.

The texture of the films has been studied in the SEM. SEM topographs of a 3.0 μm thick pure ZnO film on a textured Ag substrate are shown in Fig. 11. For comparison, the picture for the Ag substrate is shown in the same figure. The ZnO films possess a larger surface texture as shown in Fig. 11, which is probably responsible for the improved light scattering.

Doped ZnO (~ 4 at.% In)/textured Ag composite films have been used as back reflectors for the fabrication of a-Si:H cells. The thickness of the ZnO films is ~ 0.5-1.0 μm. For comparison, cells have been made in the same run on textured Ag films with no ZnO. The $Q(\lambda)$ measurements on these cells have shown significant improvement in the 650-800 nm region for the ZnO-based devices. The $Q(\lambda)$ traces for cells on the two types of back reflectors are shown in Fig. 12. The results establish that the chemically deposited ZnO film on the Ag back reflector is providing the necessary texture for Jsc enhancement primarily due to improved response in the long wavelength region.

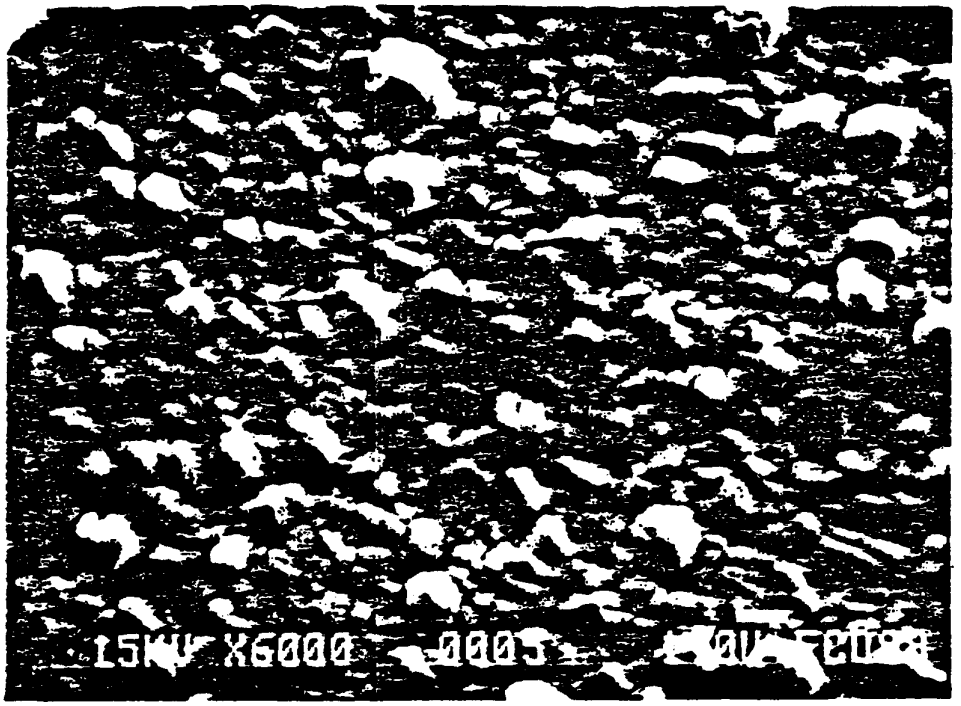

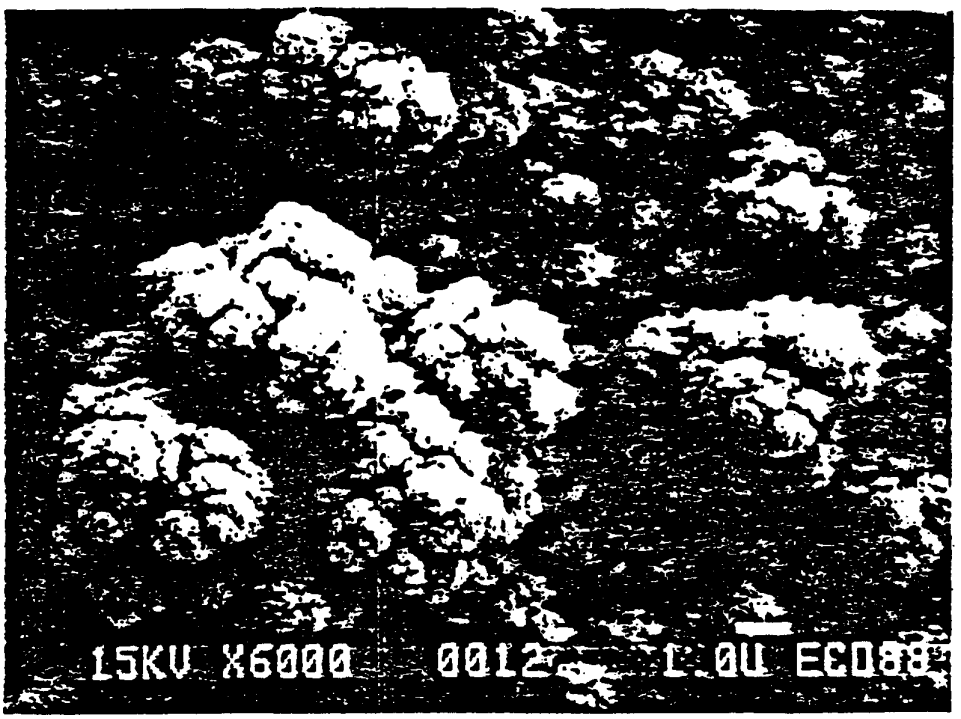

Fig. 11. SEM topograph of (a) textured Ag substrate and (b) ZnO on textured Ag substrate. The magnification is 6000X for both pictures.

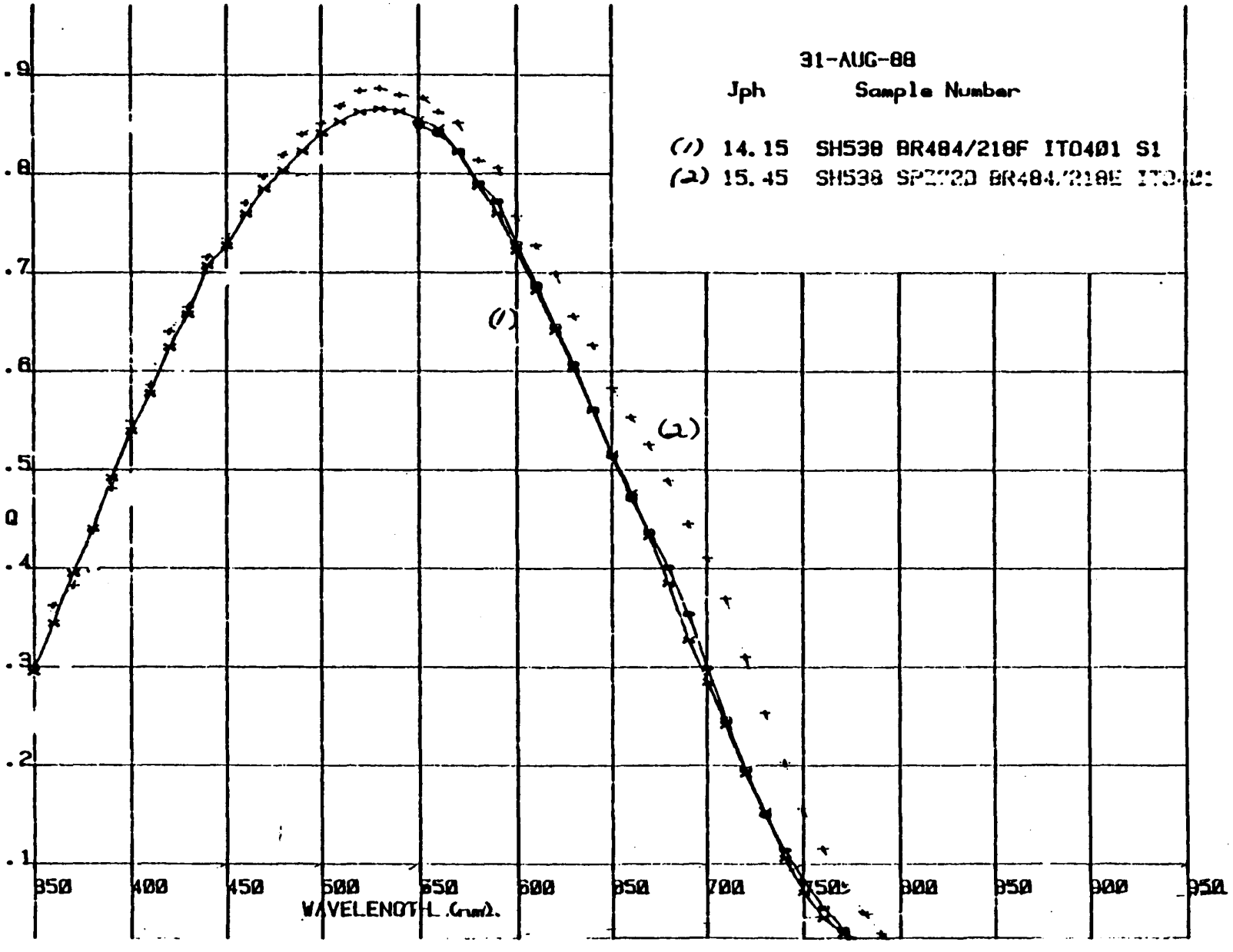

Fig. 12. Q(λ) of two cells prepared under identical conditions in the same run: (1) on textured Ag substrate and (2) on chemically deposited ZnO/textured Ag substrate.

SECTION 3

DEVICE PHYSICS AND COMPUTER MODELING

3.1. INTRODUCTION

As we have discussed earlier, improved material quality, both for the doped layers and the narrow band-gap alloys, plays a key role in increasing device efficiency. While substantial progress has been made in these areas, we also have been exploring the possibility of improving efficiency by suitable cell architecture. In this section, we discuss the details of a cell structure which allows us to obtain higher efficiency by using internal fields to aid carrier transport in the bulk of the material. We also discuss the numerical modeling of a-Si alloy solar cells that we have now developed to consider both single- and multi-junction cells.

3.2 CELL DESIGN

Several cell designs have been reported in the past [1,2] where grading or buffer layers have been incorporated at the junction interface to reduce carrier recombination near the junction. We have investigated profiling the composition of the a-Si:Ge alloy throughout the bulk of the intrinsic material so as to have a built-in electrical field in a substantial portion of the intrinsic layer. Different types of profiling configurations are shown in Fig. 13. Let us first consider two simple cases in which 1) the band gap is minimum at the p-i interface through which light enters and increases linearly away from the interface (normal profiling), and 2) the band gap is maximum at the p-i interface and decreases away from it (reverse profiling). From band structure considerations, assuming that both the conduction and the valence band edge positions shift equally as Ge is incorporated in the material, intuitively one would expect that normal profiling will help hole transport and make electron transport more difficult. The opposite will be the case for reverse profiling. Since hole transport is the limiting factor determining a-Si alloy solar cell performance, one would therefore expect an improvement in fill factor for the case of normal profiling. However, since the open-circuit voltage of the solar cell is determined by the major junction [3] which is at the p-i interface, one expects a higher open-circuit voltage for the reverse profiling case where the band-gap for the i-layer at the p-i interface is larger.

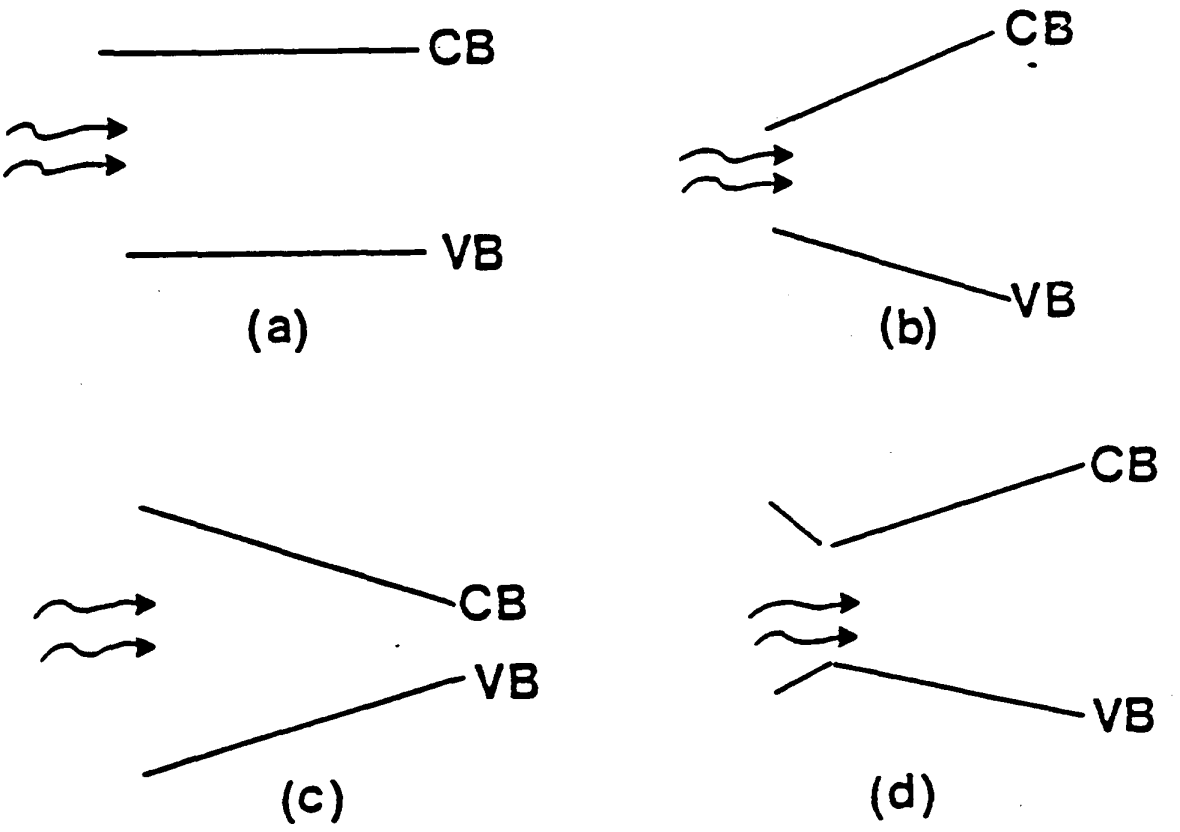

Fig. 13. Band-gap profiling for the cases of a) no profiling, b) normal profiling, c) reverse profiling and d) double profiling.

Using our computer simulation model developed for amorphous silicon alloy p-i-n solar cells [4,5], we have studied the performance of devices using structures with and without band-gap profiling. Results for red light incident on the cells are shown in Table II. As discussed above, the computer simulation does demonstrate that for similar short-circuit currents (Jsc), the fill factor (FF) is enhanced for normal profiling, and the open-circuit voltage (Voc) is increased for reverse profiling. One can then take advantage of the two situations and use a double-profiled structure as shown in Fig. 13d. Computer simulation results (Table II) show that this gives the best performance. Both Voc and FF improve over the case when the composition is uniform. The improvement in Voc depends on the thickness of the region of reverse profiling. As the thickness increases, Voc increases; however, the FF starts decreasing at larger thicknesses since the holes now have to move against a potential barrier over a larger distance.

Table II. Simulated results for a-Si:Ge alloy solar cells with different types of profiling. The results are for red light illumination.

	Constant Band Gap 1.52 eV	Normal Profiling 1.52--1.72 eV	Reverse Profiling 1.72--1.52 eV	Double Profiling
Jsc (mA/cm^2)	1.64	1.51	1.57	1.55
Voc (volts)	0.67	0.70	0.76	0.72
FF	0.55	0.65	0.44	0.64
Power (mW/cm^2)	0.62	0.68	0.52	0.71

The above analysis shows that it is possible to improve the performance of solar cells by using suitable structure designs even though the material quality remains the same. It should be mentioned that we have considered above the simplest cases. It is possible to achieve further improvement in cell efficiency by suitable non-linear and multiple-profiling which will give rise to maximum internal field.

3.3. NUMERICAL MODELING

3.3.1. INTRODUCTION

The amorphous silicon alloy device model which we have previously used to describe the effects of amorphous and microcrystalline contacts, buffer layer and the dominant junction on device performance has been updated and modified. The new program predicts the behavior of single- or multi-junction devices with constant or graded intrinsic regions, under global AM1.5 or monochromatic illumination. The optical generation rate has been extended for sub-band-gap absorption and it also takes into account multiple scattering of the red light within the cell. To get a better agreement between the open-circuit voltages of simulated and experimental data, we represented the mobility gap as an empirical function of optical band gap. The device model has also been modified to account for external parasitic series and shunt resistances.

3.3.2. DEVICE MODEL

The optical and transport properties of the device are mainly affected by the band-gap modification and doping. This is accurately described by a four-exponential model of the localized gap and tail state density (Fig. 14) where the minimum density of states g_{min} is dependent, through an empirical function, on optical band gap and impurity concentration.

In our model the D mid-gap states are approximated with the superposition of two exponentials (Fig. 14), which follow closely the experimentally determined DOS [6,7]. The donor-like states have a characteristic slope of temperature T3=2000K, and for the acceptor-like states we have T2=1500K. The minimum density of deep states, g_{min}, is 5×10^{15} $cm^{-3}eV^{-1}$ for the a-Si:H alloy with a 1.72 eV band-gap, and increases without change of the slopes with the addition of germanium to 3.2×10^{16} $cm^{-3}eV^{-1}$ in 1.5 eV material. The position of the minimum density of localized states, E_{mc}, was assumed to be at 0.4xEg from the conduction band edge. This gives a reasonable dark conductivity for the a-Si:H alloy of 10^{-10} $(\Omega\ cm)^{-1}$.

The increase in DOS with doping is described by an empirical formula derived from the detailed steady-state photoconductivity studies [8,9,10]:

$$g_{min}(N) = g_{min}(0) + k1(N/k2)^{0.5} \qquad (1)$$

In this relation $k1=3x10^{16}$ $cm^{-3}eV^{-1.5}$ for amorphous material and $10^{15}cm^{-3}eV^{-1.5}$ for microcrystalline materials with $k2=10^{16}cm^{-3}$.

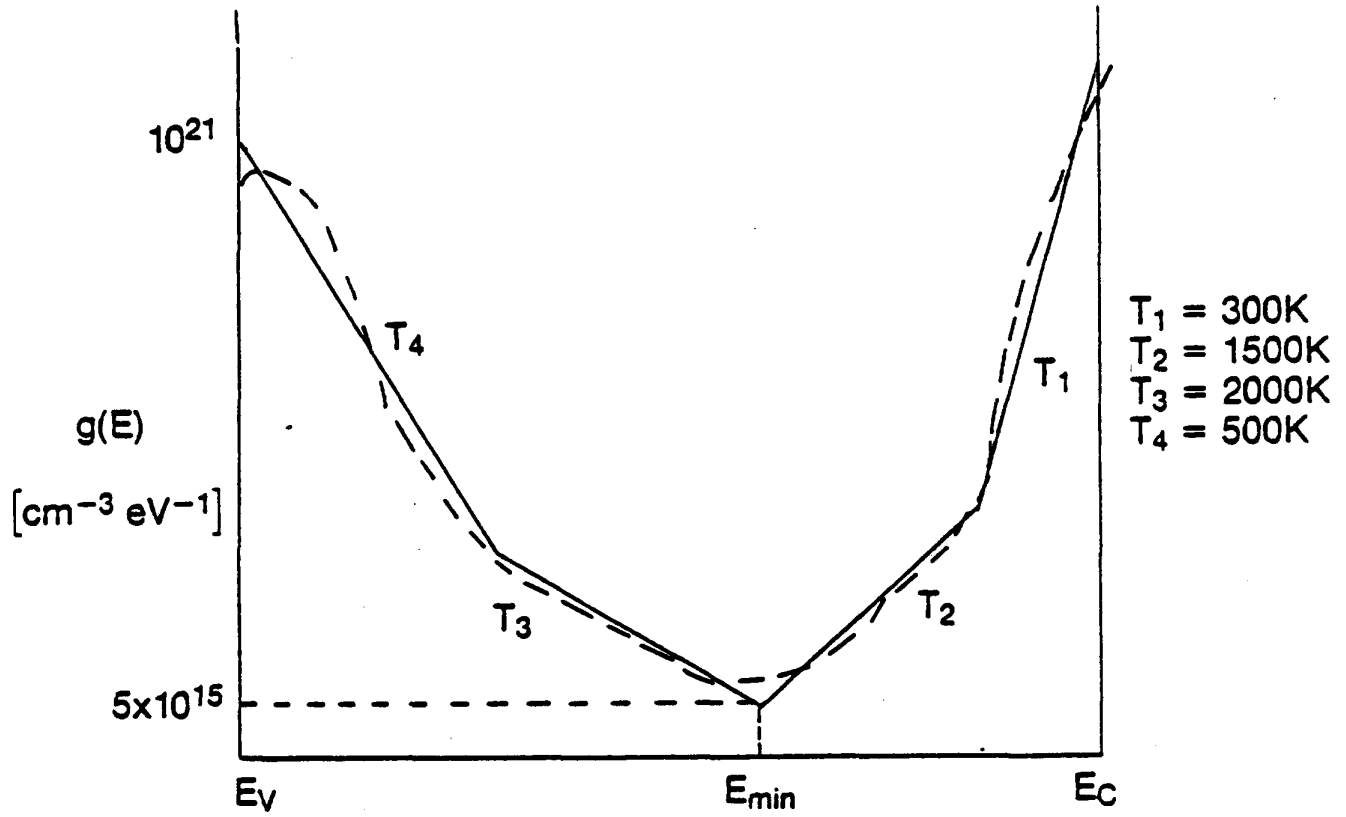

Fig. 14. Realistic density of states g(E) distribution and simplified analytic approximation used in our model.

The tail states are also represented by donor-like and acceptor-like exponential distributions with characteristic slopes of temperatures T4=500K and T1=300K, respectively. The densities of states at the bottom of the conduction and the top of the valence bands were assumed to be the same as for crystalline silicon.

One obtains the total number of trapped carriers, n_t and p_t, by integrating across the mobility gap the density of states g(E) times the probability-of-occupancy function, $f_e(E)$ for electrons and $f_h(E)$ for holes:

$$n_t = \int_{Ev}^{Ec} g_a(E) f_{ea}(E) dE \tag{2}$$

$$p_t = \int_{Ev}^{Ec} g_d(E) f_{hd}(E) dE \tag{3}$$

where

$$g_a(E) = g_{oa} \exp[(E-E_{gmin})/kT2] + g_{cta} \exp[-(E_c-E)/kT1] \tag{4}$$

and

$$g_d(E) = g_{od} \exp[-(E-E_{gmin})/kT3] + g_{vtd} \exp[(E_v-E)/kT4] \tag{5}$$

are the exponential approximations for the density of acceptor-like and donor-like localized states, respectively, with $g_{oa} = g_{od}$ gmin/2 $= 5 \times 10^{15}$ $cm^{-3}eV^{-1}$ for the deep gap states, and g_{cta}, g_{vtd} are the DOS where the acceptor-like and donor-like tail states intercept the conduction and valence bands, respectively.

To simplify calculations we have used a zero temperature distribution function f(T=0K) for trapped carriers [4]. This introduces insignificant error as shown by the excellent agreement between the simulated and experimental data for a wide temperature range [11].

In this approximation the probability of electrons occupying the acceptor-like trap states is given by:

$$f_{ea}(E) = \begin{cases} 0, & E_{tna} < E < E_c \\ n/(n+Cp), & E_{tpa} < E < E_{tna} \\ 1, & E_v < E < E_{tpa} \end{cases} \tag{6}$$

whereas the probability of holes occupying the donor-like trap states is given by:

$$f_{hd}(E) = \begin{cases} 0, & E_{tnd} < E < E_c \\ p/(nC+p), & E_{tpd} < E < E_{tnd} \\ 1, & E_v < E < E_{tpd} \end{cases} \tag{7}$$

Both trapped holes and electrons enter the Poisson's equation through the space-charge density, $\rho(x)$, where:

$$\rho(x) = q[p_t(x)-n_t(x)+N_d^+(x)-N_a^-(x)+n(x)-p(x)] \tag{8}$$

Here n(x) and p(x) are the concentrations of free electrons and holes, and $N_d^+(x)$, $N_a^-(x)$ are the concentrations of ionized shallow donors and acceptors, respectively.

The computer simulation is based on a solution (in one dimension) of Poisson's equation governing the electric potential distribution across the cell:

$$dF/dx = \rho(x)/\epsilon \tag{9}$$

along with the current continuity equations:

$$-1/q \; dJ_n/dx = G(x) - R(x) \tag{10}$$

$$1/q \; dJ_p/dx = G(x) - R(x) \tag{11}$$

where

$$J_n = q\mu_n(nF + kT/q \; dn/dx) \tag{12}$$

and

$$J_p = q\mu_p(pF - kT/q \; dp/dx) \tag{13}$$

are the electron and hole current densities (drift + diffusion), F(x) is the electric field, ε is the permittivity of the alloy material, μ_n = 10 cm^2/Vs and μ_p = 0.5 cm^2/Vs are the electron and hole band mobilities, and G(x) and R(x) are the generation and recombination rates, respectively.

The recombination rate, R(x), is based on the Shockley-Read-Hall (SRH) recombination model extended over the range of states acting as recombination centers and located between the electron and hole trap quasi-Fermi levels, E_{tna}, E_{tpa} for acceptor-like states:

$$E_{tna} = E_c + (kT \ln[(n+Cp)/Nc]) \tag{14}$$

$$E_{tpa} = E_v - (kT \ln[(p+n/C)/Nv]) \tag{15}$$

and E_{tnd}, E_{tpd} for donor-like states [4,12]:

$$E_{tnd} = E_c + (kT \ln[(n+p/C)/Nc]) \tag{16}$$

$$E_{tpd} = E_v - (kT \ln[(nC+p)/Nv]) \tag{17}$$

R(x) is given by:

$$R(x) = (pn-n_i^2)\, Cv_{th}\sigma_n \left[\int_{E_{tpa}}^{E_{tna}} g_a(E)f_{ea}(E)dE + \int_{E_{tpd}}^{E_{tnd}} g_d(E)f_{hd}(E)dE\right] \quad (18)$$

where n_i is the intrinsic carrier concentration, the n_i^2 term is responsible for thermal generation of carriers, v_{th} is the thermal velocity and σ_n is the neutral trap cross-section. For a-Si:H, σ_n is taken to be on the order of 10^{-16} cm^2 and exponentially increases to $3x10^{-16}$ cm^2 for an a-Si:Ge:H alloy with an optical band-gap of 1.5 eV. C is the ratio between the charged and neutral trap cross-sections. After Hack et al. [4] we assumed it to be 100.

A very important aspect of double- and triple-cell simulation is the accurate description of photo-excitation which depends on the optical band-gap of each cell and the energy of the photons incident on that cell. In the case of a multi-cell simulation, one has to account for the absorption in the upper cell(s) before the radiation reaches the middle or bottom devices. Since our structure has a graded intrinsic region -- and hence an optical band-gap which changes with position -- we need to calculate the absorption coefficient for each mesh point and then the corresponding generation rate. The absorption coefficient is computed for direct:

$$(\alpha h\nu)^{0.5} = \text{Const}(h\nu - \text{Eopt}) \quad (19)$$

and sub-band-gap absorption. The Const term was assumed to be $700\ cm^{-1}eV^{-0.5}$ [13]. The generation rate is computed from the following formula:

$$G(x) = \Phi(\lambda,x)\exp[-\alpha(\lambda,x)dx] \quad (20)$$

where Φ is the incident photon flux at each mesh point, already accounting for the absorption in previous layers, and dx is the mesh thickness. To account for multiple scattering of weakly absorbed red light, the generation rate is calculated from three or four light passes through the cell. Obviously, for global AM1.5 illumination this procedure must be repeated for each wavelength composing the solar spectrum.

We also included in the solar cell model the external parasitic series and shunt resistances which seriously degrade the device performance. We have assumed that external series resistance is on the order of 1 to 2 Ohms and parasitic external shunt resistance is infinitely large in high quality cells.

Finally, the heterojunction discontinuity between the wide-band-gap microcrystalline contacts and the amorphous bulk is modeled as being split equally between the conduction and valence bands. Also, the grading in the intrinsic region is assumed to be equally apportioned at both the valence and conduction band. At the heterojunction interface we assumed a surface state density of 10^{12} $cm^{-2}eV^{-1}$.

3.3.3. SINGLE-CELL SIMULATION

The solution of the full set of potential and transport equations coupled with empirical formulas depicting the realistic cell parameters leads to an excellent agreement between measured and simulated J-V characteristics of narrow- and wide-band-gap cells with different thicknesses and under various illumination conditions. In Table III we present the results of the simulation for various band-gap single-junction solar cells under global AM1.5 and monochromatic illumination and compare them to the measured J-V data. These devices have uniform intrinsic layers, i.e, no band-gap profiling. For the simulation we have assumed that microcrystalline n^+ and p^+ contacts have activation energies of 0.2 eV and optical band-gaps of 1.9 eV.

We have also simulated a number of single-junction devices fabricated in our laboratory with profiled band-gap intrinsic layers. The results of these calculations have been discussed previously. One example is the simulation of the J-V characteristics of a bottom cell with a Ge-profiled i-layer. These results are compared with the actual, measured data in Table IV.

Table III. Comparison between the experimental and simulated J-V characteristics of single-junction devices with uniform intrinsic layers for various illumination conditions and cell characteristics.

Device # 2803 Uniform intrinsic layer

Thickness = 1200 Å Eopt = 1.75 eV

Global AM1.5

Parameters	Experiment	Simulation
Voc [Volts]	0.96	0.98
Jsc [mA/cm^2]	8.14	8.27
FF	0.77	0.74
Pmax [mW/cm^2]	5.99	6.00

Device # 2727 Uniform intrinsic layer

Thickness = 6500 Å Eopt = 1.72 eV

Global AM1.5

Parameters	Experiment	Simulation
Voc [Volts]	0.93	0.94
Jsc [mA/cm^2]	13.58	14.13
FF	0.62	0.59
Pmax [mW/cm^2]	7.80	7.82

Yellow light

Parameters	Experiment	Simulation
Voc [Volts]	0.90	0.92
Jsc [mA/cm^2]	7.76	7.84
FF	0.59	0.57
Pmax [mW/cm^2]	4.13	4.10

Table III. (cont.)

Device # 2726 Uniform intrinsic layer

Thickness = 3000 Å Eopt = 1.55 eV

Global AM1.5

Parameters	Experiment	Simulation
Voc [Volts]	0.79	0.79
Jsc [mA/cm^2]	14.01	13.97
FF	0.62	0.61
Pmax [mW/cm^2]	6.83	6.76

Red light

Parameters	Experiment	Simulation
Voc [Volts]	0.73	0.73
Jsc [mA/cm^2]	3.43	3.43
FF	0.57	0.58
Pmax [mW/cm^2]	1.43	1.45

Device # 2718 Uniform intrinsic layer

Thickness = 3000 Å Eopt = 1.47 eV

Global AM1.5

Parameters	Experiment	Simulation
Voc [Volts]	0.71	0.71
Jsc [mA/cm^2]	15.07	15.02
FF	0.55	0.56
Pmax [mW/cm^2]	5.94	5.95

Red light

Parameters	Experiment	Simulation
Voc [Volts]	0.66	0.66
Jsc [mA/cm^2]	4.64	4.61
FF	0.50	0.51
Pmax [mW/cm^2]	1.51	1.52

Table IV. Graded single-junction device with i-layer Eopt ranging from 1.72 to 1.52 to 1.72 eV.

Monochromatic red light

Parameter	Experiment	Simulation
Voc [Volts]	0.63	0.63
Jsc [mA/cm^2]	2.19	2.17
FF	0.57	0.57
Pmax [mW/cm^2]	0.79	0.78

Monochromatic blue light

Parameters	Experiment	Simulation
Voc [Volts]	0.65	0.65
Jsc [mA/cm^2]	2.24	2.35
FF	0.66	0.62
Pmax [mW/cm^2]	0.95	0.94

3.3.4. RESULTS OF TRIPLE-CELL SIMULATION

Below we present the data from the computer simulation of a state-of-the-art, triple-junction, 13.6% cell fabricated in our laboratory. The simulated J-V characteristics and band-gaps of the intrinsic regions are shown in Table V. The top and middle cells, made from a-Si:H material, had conventional, uniform band-gaps. The bottom, a-Si:Ge:H alloy cell, had an optimized band-gap profiling in its i-layer, as discussed above and in other sections of this report. The microcrystalline n^+ and p^+ contacts were 100 Å thick, their activation energies were 0.2 eV and their optical band-gap was assumed to be 1.9 eV.

Table V. Simulated triple-junction solar cell (13.6%) under global AM1.5 illumination.

Parameter	"blue" cell	"green" cell	"red" cell	total
Jsc [mA/cm^2]	7.42	7.94	8.88	
Voc [Volts]	0.99	0.92	0.67	2.58
FF	0.77	0.61	0.57	
Pmax [mW/cm^2]	5.68	4.49	3.43	13.60
Vmax [Volts]	0.87	0.70	0.53	2.10
Jmax [mA/cm^2]	6.45	6.45	6.45	6.45
Eopt [eV]	1.75	1.72	graded (1.72 > 1.45 <1.72)	

Table VI shows the measured J-V characteristics of the actual, 13.6% cell. Although limited to individual cells' photocurrents, the data agree very well with the simulated results. Also, the overall performance of the experimental device fits quite well with the numerical J-V characteristics.

Table VI. Measured triple solar cell (13.6%) under global AM1.5 illumination.

Parameter	"blue" cell	"green" cell	"red" cell	total
Jsc [mA/cm^2]	7.35	7.42	8.80	7.64
Voc [Volts]	--	--	--	2.54
FF	--	--	--	0.70
Pmax [mW/cm^2]	--	--	--	13.6
Vmax [Volts]	0.87	0.70	0.53	2.11
Jmax [mA/cm^2]	6.45	6.45	6.45	6.45

Having thus established the credibility of our model to simulate the multi-junction cell, we may concentrate on the optimization of the overall triple structure.

3.3.5. PROPOSED MODIFICATION IN TRIPLE SOLAR CELL ARCHITECTURE TO OPTIMIZE THE OVERALL EFFICIENCY

In the discussions above, we have considered the cases when only the bottom cell incorporated Ge. Since the double-profiled bottom cell can deliver much greater currents, thus giving more power through more efficient utilization of the red portion of the global AM1.5 spectrum, one may try to match this current in the other component cells of the device by either decreasing the band-gap or increasing the thickness of the top and middle cells. We opted for a thicker, 1000 Å, "blue" (top) cell, which is still thin enough to avoid serious fill factor degradation, and a double-profiled, (1.72eV > 1.59eV < 1.72eV), thinner middle cell. The bottom cell was also double-profiled with its i-layer band-gap ranging from 1.72eV to 1.35eV and back to 1.72eV.

The simulated J-V data for this structure are shown in Table VII. In Figs. 15a, b and c, one sees individual-cell J-V characteristics of the proposed architecture compared to the simulated 13.6% cell. The top cell has greater current while the Voc and FF do not suffer too much. Conversely, the middle cell loses some of the open-circuit voltage, but gains in short-circuit current and fill factor. The bottom device does not contribute any increase in power over the 13.6% red cell, due to the relatively poorer quality of the a-Si:Ge:H, 1.35 eV alloy. Nevertheless, the FF of the proposed red cell is made better than the actual 13.6% "red" cell by compensating for the worse short-circuit current and open-circuit voltage. The overall efficiency of 14.34% could be obtained with this design without any improvements in the material quality of present low band-gap alloys. Any further progress in material quality would be reflected in even greater device efficiency.

Table VII. J-V characteristics of a proposed triple-cell configuration.

Parameter	"blue" cell	"green" cell	"red" cell	total
Jsc [mA/cm^2]	8.27	9.25	8.28	
Voc [Volts]	1.01	0.85	0.61	2.45
FF	0.77	0.63	0.61	
Pmax [mW/cm^2]	6.45	4.85	3.04	14.34
Vmax [Volts]	0.95	0.71	0.45	2.11
Jmax [mA/cm^2]	6.80	6.80	6.80	6.80

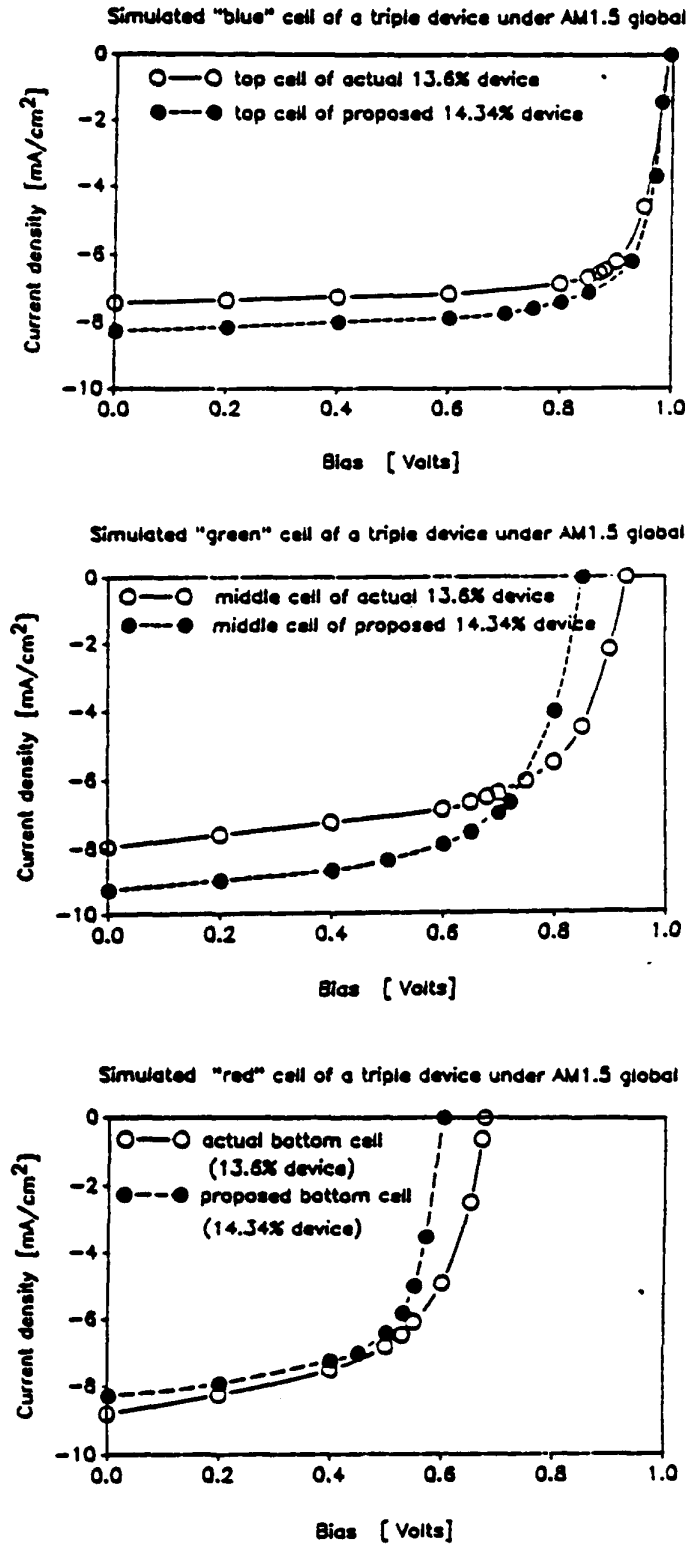

Fig. 15. Simulated J-V characteristics of solar cell components of an actual (13.6%) triple device and proposed (14.34%) structure.

3.4. CONCLUSIONS

We have presented the a-Si based solar cell model which allows for:

* Single, double or triple solar cell simulation;

* Spatial, optical and mobility band-gap variation in each cell;

* Differentiation between the amorphous and microcrystalline materials, and appropriate modeling of them;

* Calculation of the photogeneration rate from direct and sub-band-gap absorption, for monochromatic and global AM1.5 illumination, with multiple light scatterings;

* Parasitic resistances, Rser and Rshunt, external to the device;

* Realistic accounting for the worsening of transport parameters with band-gap narrowing, doping and recombination at the hetero-interfaces.

We have shown that there is an excellent agreement between the simulated and measured J-V characteristics of experimental devices with various optical band-gaps (1.75 to 1.47 eV), thicknesses and different illumination conditions. The model also gives good agreement with experimental results for triple-cell structures.

We also discussed a novel cell design which allows us to obtain higher efficiency from cells by suitable profiling of the optical band-gap in the intrinsic layer. Finally, we showed that using the novel architecture and presently available materials, it is possible to obtain 14.34% efficiency using the triple-cell configuration.

SECTION 4
DEVICE OPTIMIZATION AND STATUS

4.1. INTRODUCTION

Using the concepts outlined in the previous sections, we have optimized both single and multi-junction devices. We have also developed a new grid design which reduces the difference between total- and active-area efficiencies. The results are described below.

4.2. OPTIMIZATION OF GRID DESIGN

In order to minimize the difference between the total- and active-area efficiencies of our devices, we have developed a model which will optimize the effectiveness of our grid pattern in terms of device total-area efficiency while minimizing the loss in active-area efficiency. The model is completely general and can consider any type of device, single- or multi-junction, any range of TCO or metallization resistivities, and any device and finger geometry.

The general approach was to divide the device, mathematically, into tiny current elements, as shown in Fig. 16. Each of these current elements may have its own I-V characteristic, i.e., light I-V curve for TCO element or dark I-V for grid element, as well as its own sheet resistivity. The size of each current element is dictated by the resolution needed to model the smallest features on the surface, in this case the minimum width of a finger, which was taken to be five thousandths of an inch.

We next applied a voltage bias at some point on the device, e.g., the contact pad, and then raised the operating voltage of each current element until Kirchoff's equations were satisfied for each current element. In this case, we have:

$$A_{i,j} \times J_{i,j}(V) - \sum_{x=i-1}^{i+1} \sum_{y=j-1}^{j+1} (V_{i,j}-V_{x,y})/R = 0 \qquad (21)$$

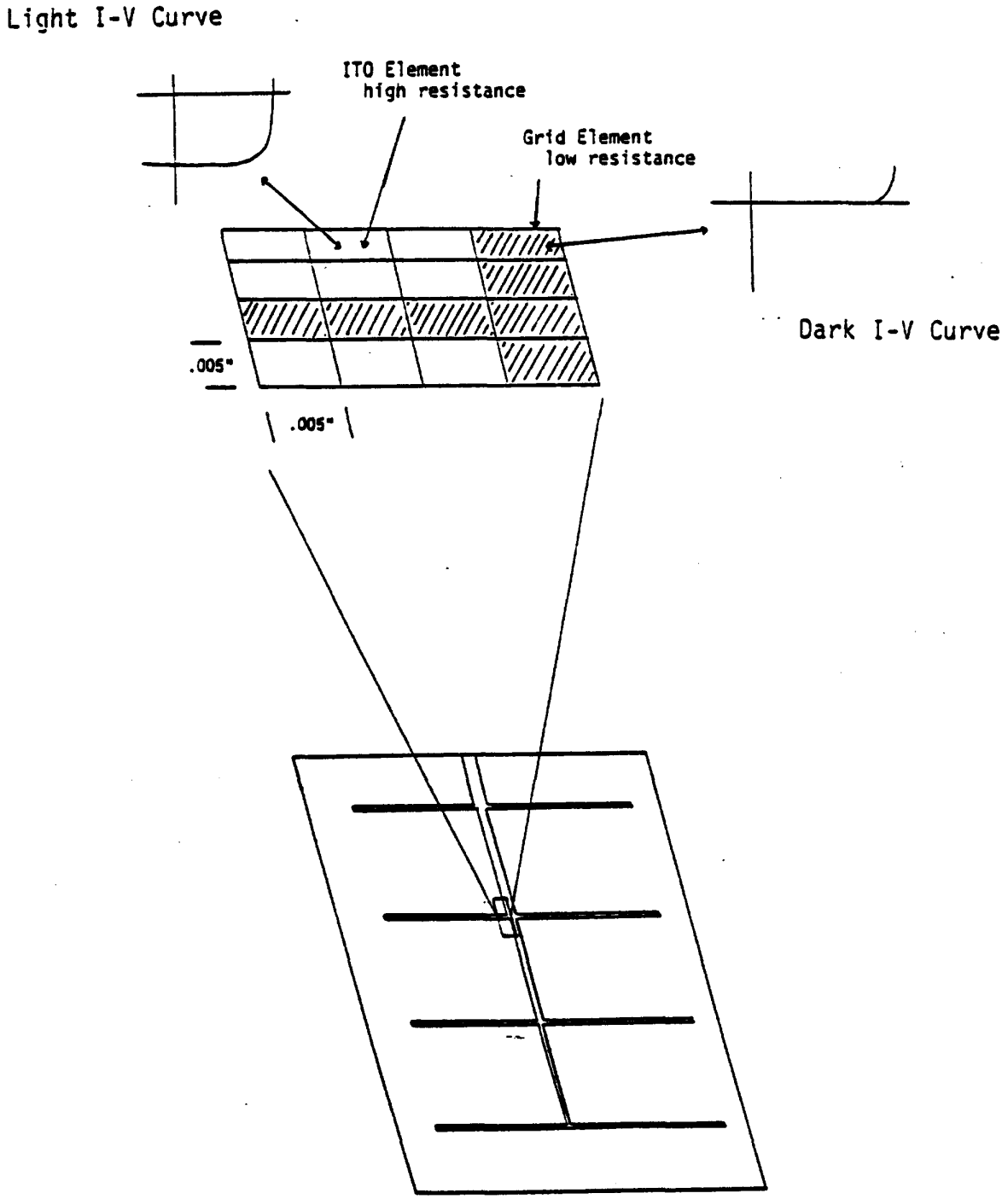

Fig. 16. Schematic drawing of a photovoltaic device used in the grid-design optimization model, showing the I-V characteristics of the ITO- and grid-covered regions.

where the first term is the generated current in the device, $A_{i,j}$ is the area of element (i,j), and $J_{i,j}(V)$ is the current density of element (i,j) at voltage, V. The second term is the sheet current where $V_{i,j}$ is the operating voltage of element (i,j), $V_{x,y}$ the operating voltage of an adjacent element (x,y), and R is the resistivity between (i,j) and (x,y) given by:

$$R \simeq 8\,[(\rho_{\square}/2\pi)\,\ln(3(d/2)/(d/2))] = 1.40\rho_{\square} \qquad (22)$$

where $\rho_{\square}$ is the sheet resistance of the current element.

In Fig. 17 we see our present finger pattern. The rectangular pattern is the border between TCO and metallization. The curved lines represent lines of equal potential and are calculated from the model and labeled in mV with respect to the contact point which is arbitrarily set to zero volts. (Only half of the device is shown due to exact symmetry.) The underlined values are experimentally determined and, as one can see, agree quite well with the calculated values. The sheet resistivities were 160 Ω/□ for the TCO and 0.17 Ω/□ for the metallization. The gradient of the equipotential lines determines the path of current flow and, as can be seen, is quite indirect with respect to the grid. Most of the device is operating within 10 mV of the contact voltage; this is unnecessarily small for a 7 mA, 2.5 volt device (i.e., our triple-junction cells). The grid coverage here is about 8% of the total area and the active-area efficiency loss is less than 0.5%.

We then optimized the finger pattern for total-area efficiency while minimizing active-area efficiency losses and arrived at the pattern shown in Fig. 18. We used the same sheet resistivities as in the previous case. The voltage drops across the device are now much more in line with what would be expected from our optimized high-voltage triple-junction devices. Note the lines of equal potential run much more parallel to the metallization, resulting in a direct current flow to the grid finger. This pattern results in a 2.5% difference between total- and active-area efficiency. The total area efficiency is increased by 5% over the pattern in Fig. 17 while the active-area efficiency is decreased by just 1%.

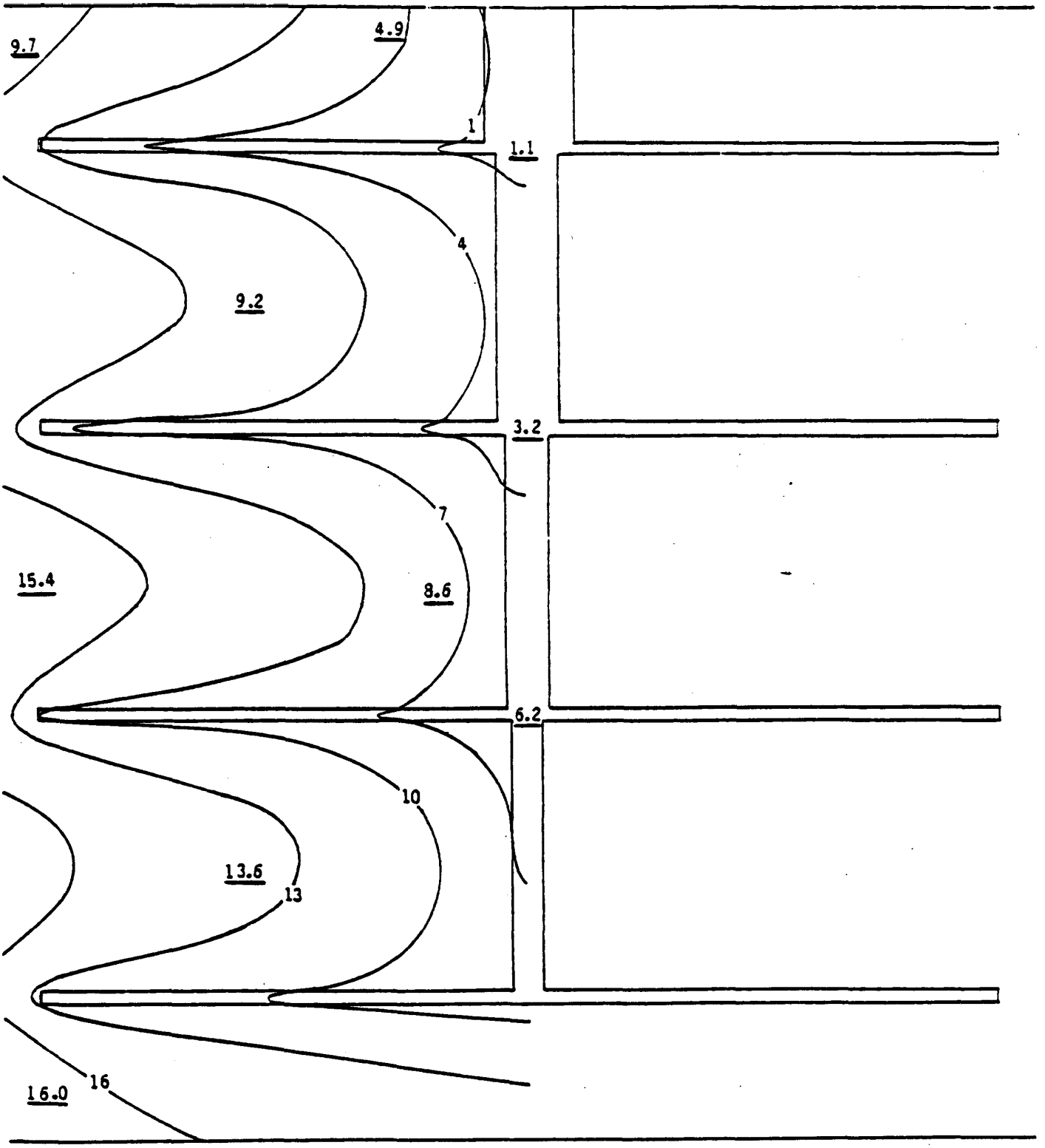

Fig. 17. The present grid design, showing the grid pattern with fingers and equal potential lines. The voltages are in mV with respect to the potential at the contact pad.

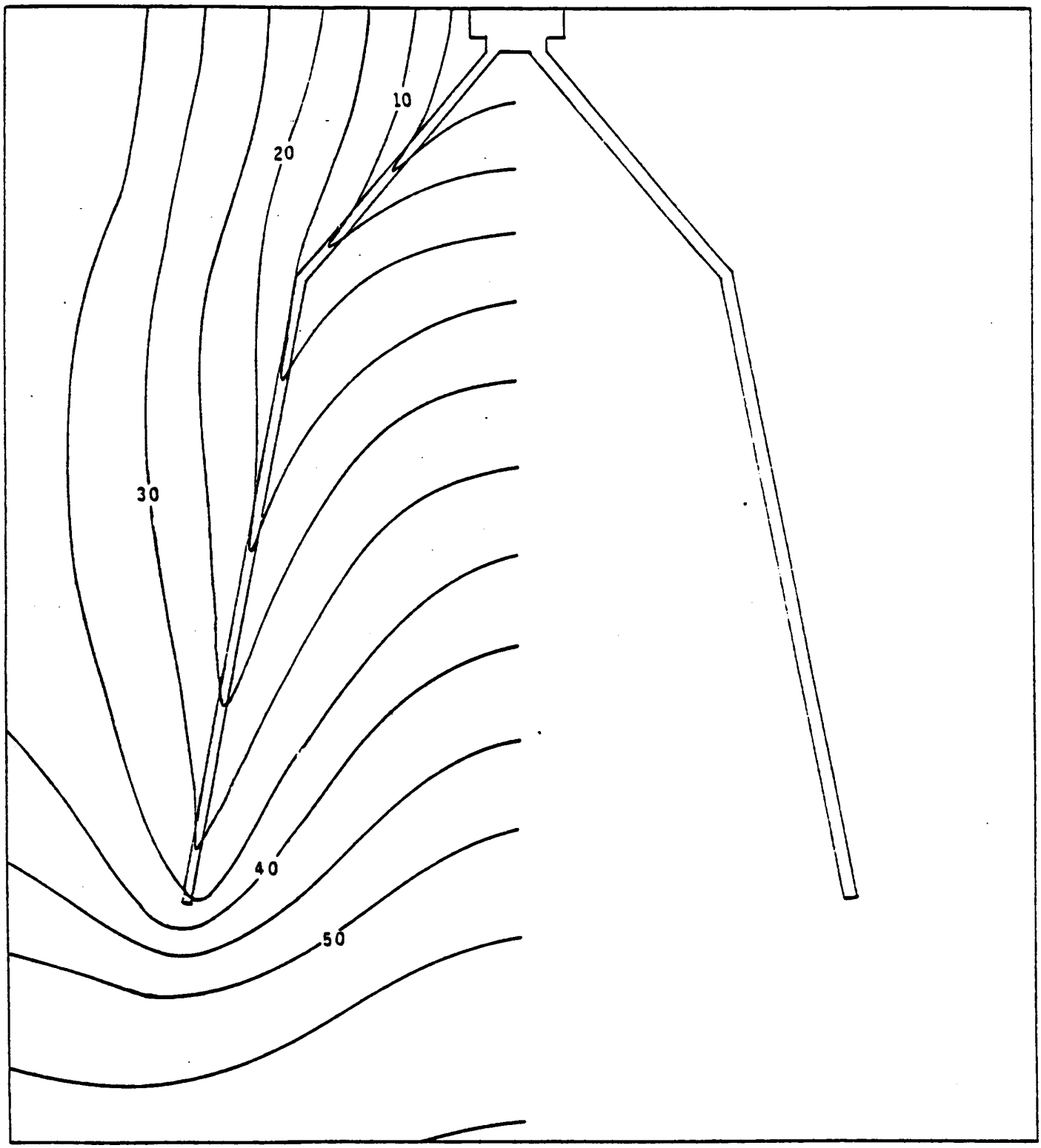

Fig. 18. The new grid design, optimized for high voltage triple-junction devices, and designed to maximize total-area efficiency while minimizing active-area efficiency losses.

4.3. INTRINSIC LAYERS WITH BAND-GAP PROFILING

As we have discussed in Section 3, band-gap profiling in the intrinsic layer can be used to increase the efficiency of a-Si:Ge alloy devices. It offers the opportunity to modify the generation-recombination rate profiles in the i-layer along with the ability to introduce electric fields by electron affinity grading. Each of these phenomena affects the Voc and FF of the graded band-gap device. The generation-recombination rate profile determines how far, on average, a carrier must travel to be collected or to recombine. The affinity grading introduces electric fields which add to the existing electric field within the device caused by the space charge. The affinity electric field, which can be in any direction, can either help or hinder the transport of free carriers; it depends on whether or not the net field is increased or decreased by the affinity grading.

Several solar cells with graded band-gap intrinsic layers have been fabricated in our laboratory. They have been produced by the glow discharge decomposition of germane (GeH_4) and disilane (Si_2H_6) gases with a hydrogen (H_2) dilution and an r.f. excited plasma. The silicon to germanium concentration ratio in the bulk is varied by changing the mass flow ratio of disilane to germane. In this manner, the optical band-gap of the resulting alloy material can be accurately and reproducibly controlled. The germanium concentration in the bulk was determined by Auger analysis, and the optical band-gap was determined by quantum efficiency and reflection measurements of uniform band-gap samples on stainless steel substrates.

For the purpose of this study, we have fabricated several a-Si:Ge alloy devices. The band-gap profiles of these devices are shown in Fig. 19. These sketches are meant to be used only to indicate the structure of the device. No attempt has been made to include band bending in the diagrams. All of the samples are deposited on stainless steel and include 200Å n^+ and 100Å p^+ contact (doped) layers and 600Å of ITO as a TCO and AR coating. Samples L2722, L2723 and L2726 all have 3000Å intrinsic layers of silicon-germanium alloy.

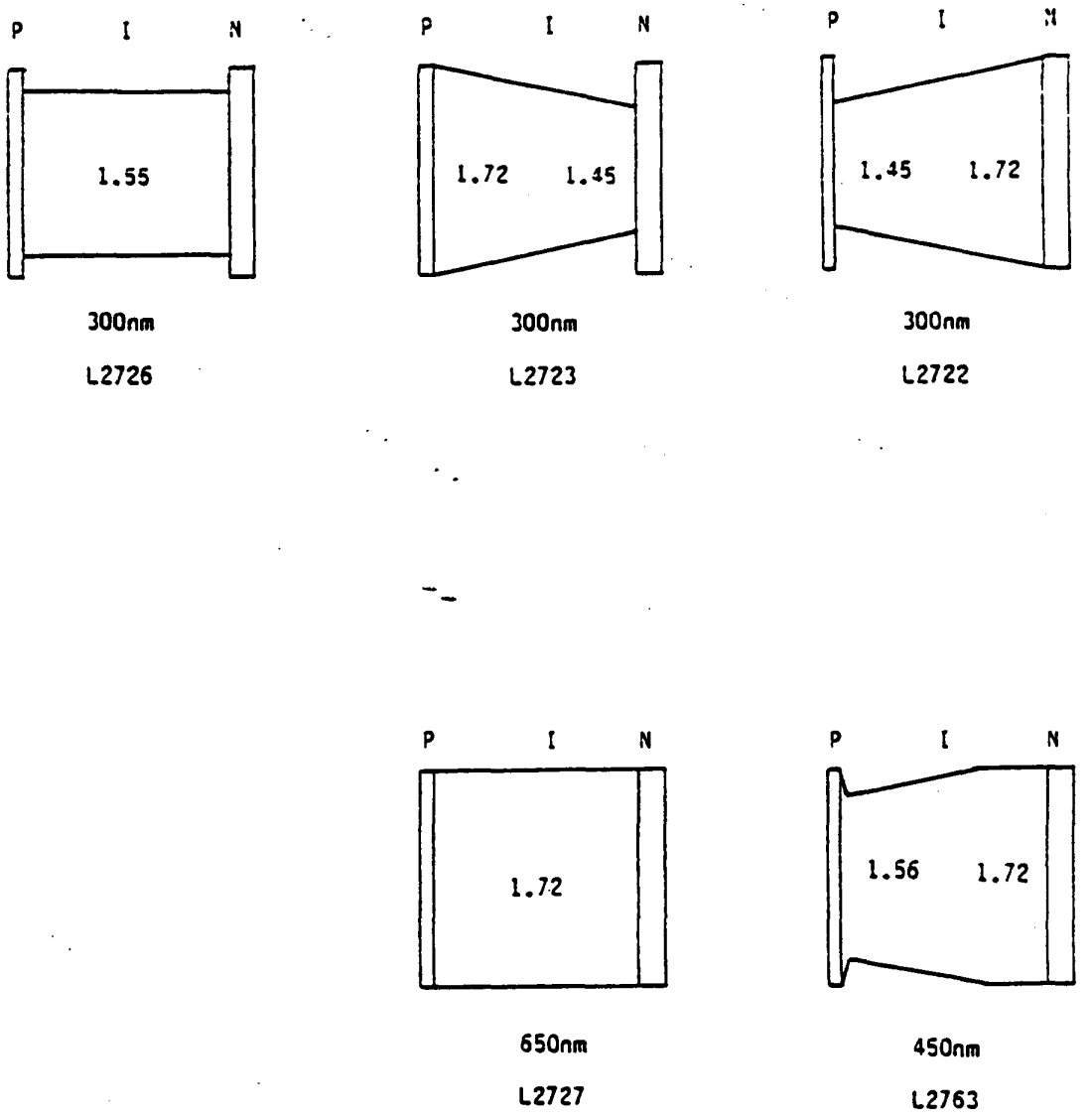

Fig. 19. Schematic band diagrams of various a-Si and a-Si:Ge alloy n-i-p devices showing the band-gap profiles across the intrinsic layer.

Sample L2727 has a 6500Å silicon intrinsic layer while L2763 has a 4500Å silicon-germanium alloy intrinsic layer. Samples L2726, L2723 and L2722 are used to illustrate the general effect band-gap profiling has on device performance. Samples L2727 and L2763 are used to study grading in the middle cell of a triple device.

Figure 20 shows the J-V characteristics of samples L2726, L2723 and L2722 under both AM1.5 and red illumination. It is readily apparent from these data that the device with the wider band-gap nearest the p^+ region (L2723) has the highest Voc while the device with the narrow gap near the p^+ region (L2722) has the highest FF. Figure 21 shows the dark current-voltage characteristics of the same three devices. From these data one can see that the higher Voc is due to the decreased slope of the dark forward characteristic.

These results can be explained in a consistent manner by using the following simple model. Consider the device with the narrowest gap material near the p^+ contact. Since the density of states is highest near the p^+ region, the point in the device where the recombination rate is the greatest is shifted towards the p^+ contact. Thus the average distance that an injected hole travels before recombining is reduced and a larger current can flow at a given forward bias. This effect tends to reduce the Voc. However, since the narrowest gap material is nearest the p^+, the average distance that holes travel is reduced and the FF is improved. The affinity grading also provides an electric field that tends to help holes traverse the bulk of the intrinsic layer, thus providing additional improvement in the carrier collection and FF.

In order to increase the current from the triple device, it is necessary to increase the current from the middle cell. This can be achieved by increasing the thickness or decreasing the band-gap of the middle-cell i-layer. Of these two alternatives, the reduction of the band-gap is the most desirable, since obtaining a significant increase in current by increasing thickness would require the middle intrinsic layer to become much too thick to efficiently extract carriers. In Fig. 19 we showed a 6500Å amorphous silicon device, L2727, and a 4500Å silicon-germanium alloy device, L2763. This germanium alloy device

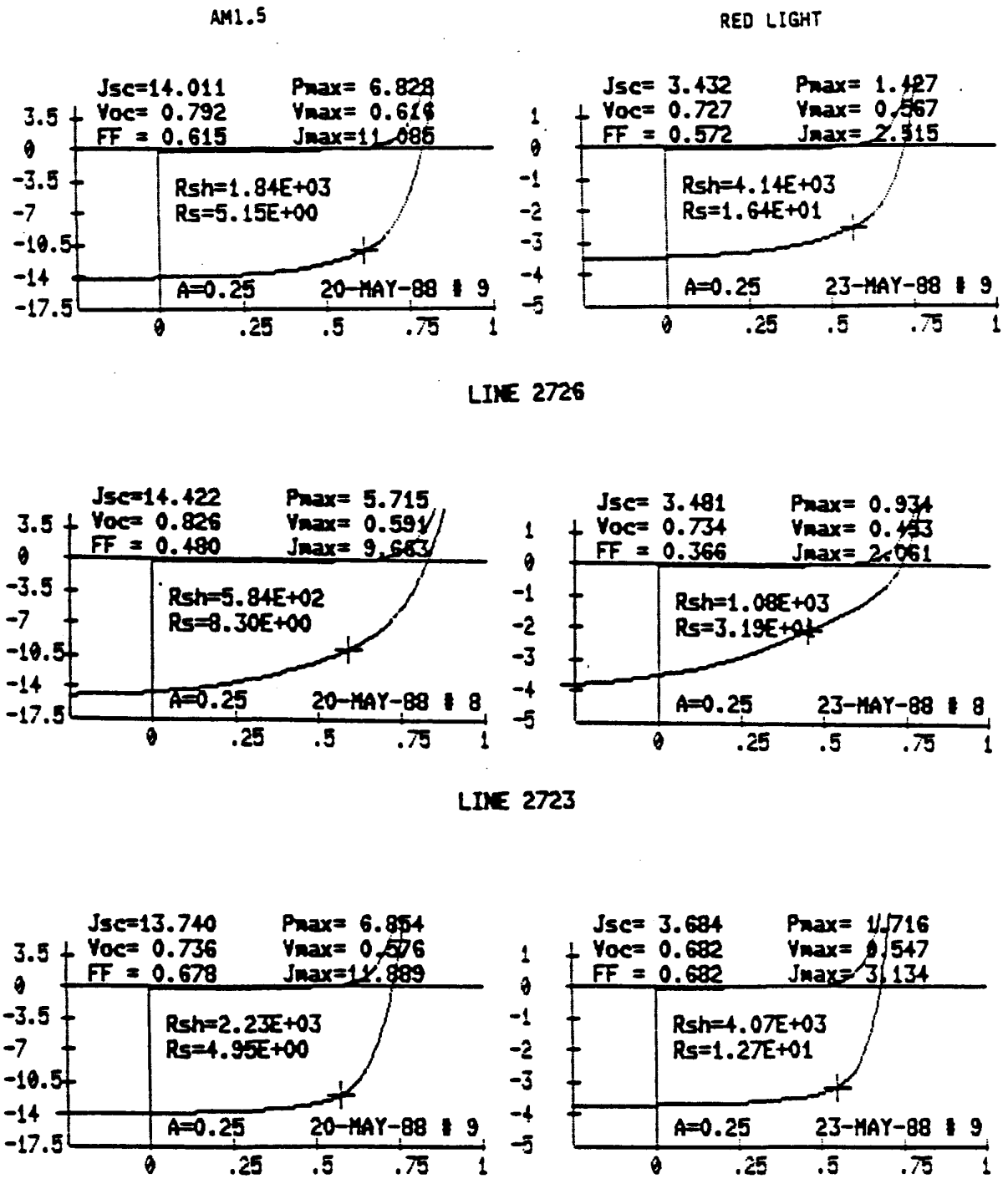

Fig. 20. The J-V characteristics under AM1.5 and red-light illumination of three a-Si alloy devices with varying amounts of band-gap profiling in their intrinsic layers (see Fig. 19 for the band-gap profiles).

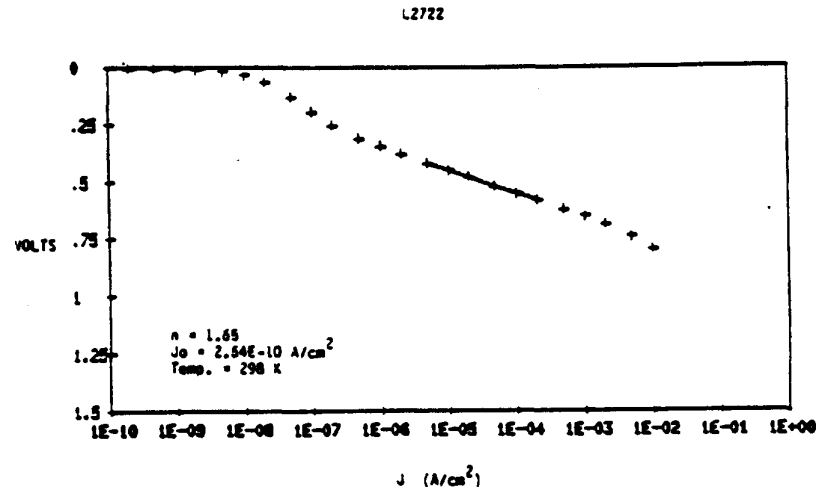

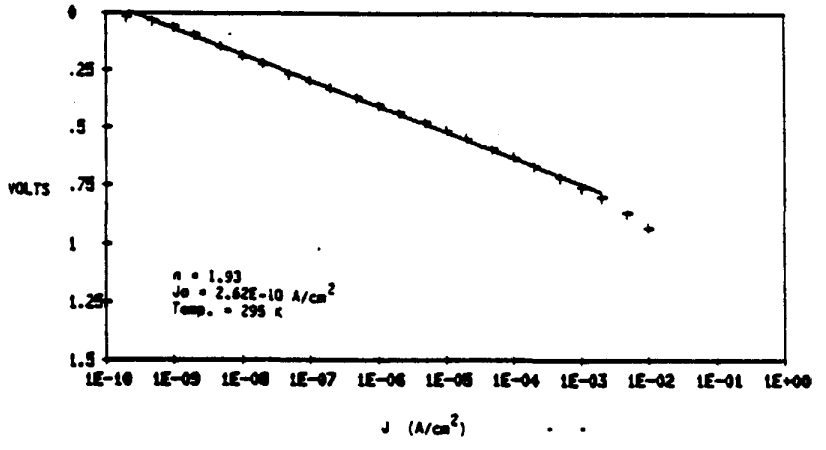

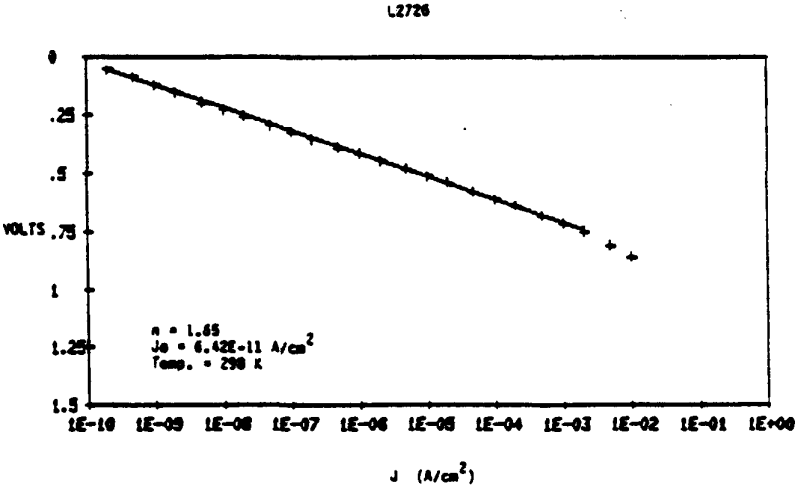

Fig. 21. The dark log J-V characteristics for the three a-Si alloy devices in Fig. 20.

has 1500Å of a:Si:H on top of the n^+ layer followed by 3000Å of linearly-graded germanium alloy. The band-gap decreases from 1.72 eV at the n^+i interface to 1.55 eV near the p^+i interface. The device also has a linearly graded top buffer region to improve the Voc. The J-V characteristics of these devices is shown in Fig. 22. Here we show the AM1.5 and yellow light characteristics. The yellow light is chosen to simulate the type of illumination present in the middle of a triple-stacked cell. As one can see from the data, the germanium alloy device is not as efficient under white light; it is, however, more efficient under yellow light. This is primarily due to the enhanced FF of the alloy device. It is this type of graded band-gap middle cell that is being used to increase the efficiency of our triple-stacked multi-junction devices.

4.4. DICE RESULTS

A very useful tool in evaluating the effect of band-gap profiling on device performance is the measurement of the internal collection probability versus position within the graded intrinsic layer. This measurement was introduced by Takahama et al. [14] and referred to as the Dynamic Internal Collection Efficiency (DICE). By definition, this quantity is defined as the probability that an electron-hole pair generated at a particular depth gets collected and contributes to the external current. This probability is deconvoluted from the quantum efficiency measurement at various applied voltages along with optical data on each device.

In Fig. 23 we show the collection probability function versus intrinsic-layer position for samples L2722, L2723 and L2726. In general we see a probability near unity through most of the intrinsic-layer with the it falling near the p^+i and n^+i interfaces. The drop in the probability near the p^+i interface is attributed to electron transport through the device, while the drop near the n^+i interface is due to hole transport through the device. We can see quickly that there is very little change in the probability near the p^+i interface due to the various affinity gradings. Hence, this grading has very little effect on electron transport. This is not the

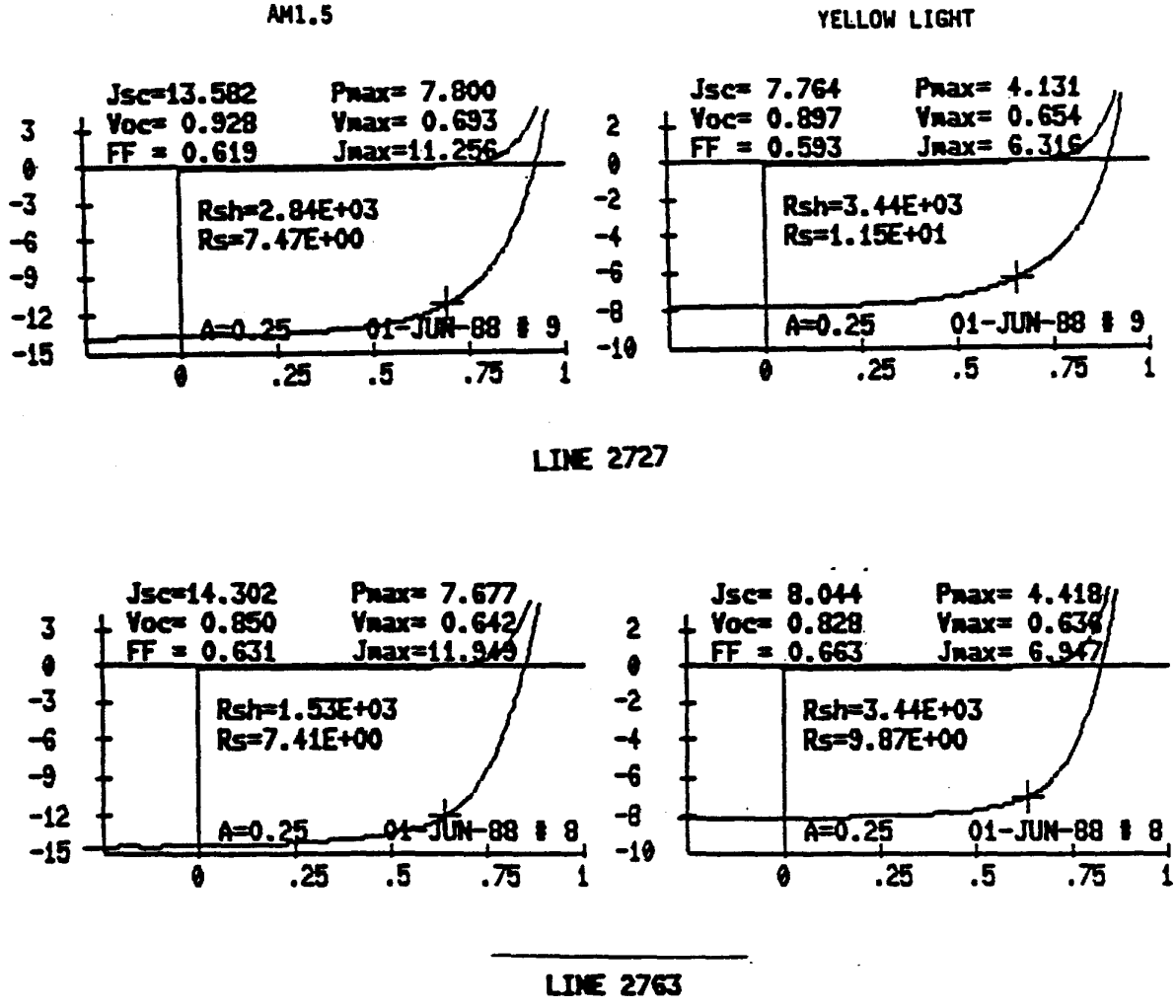

Fig. 22. The J-V characteristics under AM1.5 and yellow-light illumination of two a-Si alloy devices with varying amounts of band-gap profiling in their intrinsic layers (see Fig. 19 for the band-gap profiles).

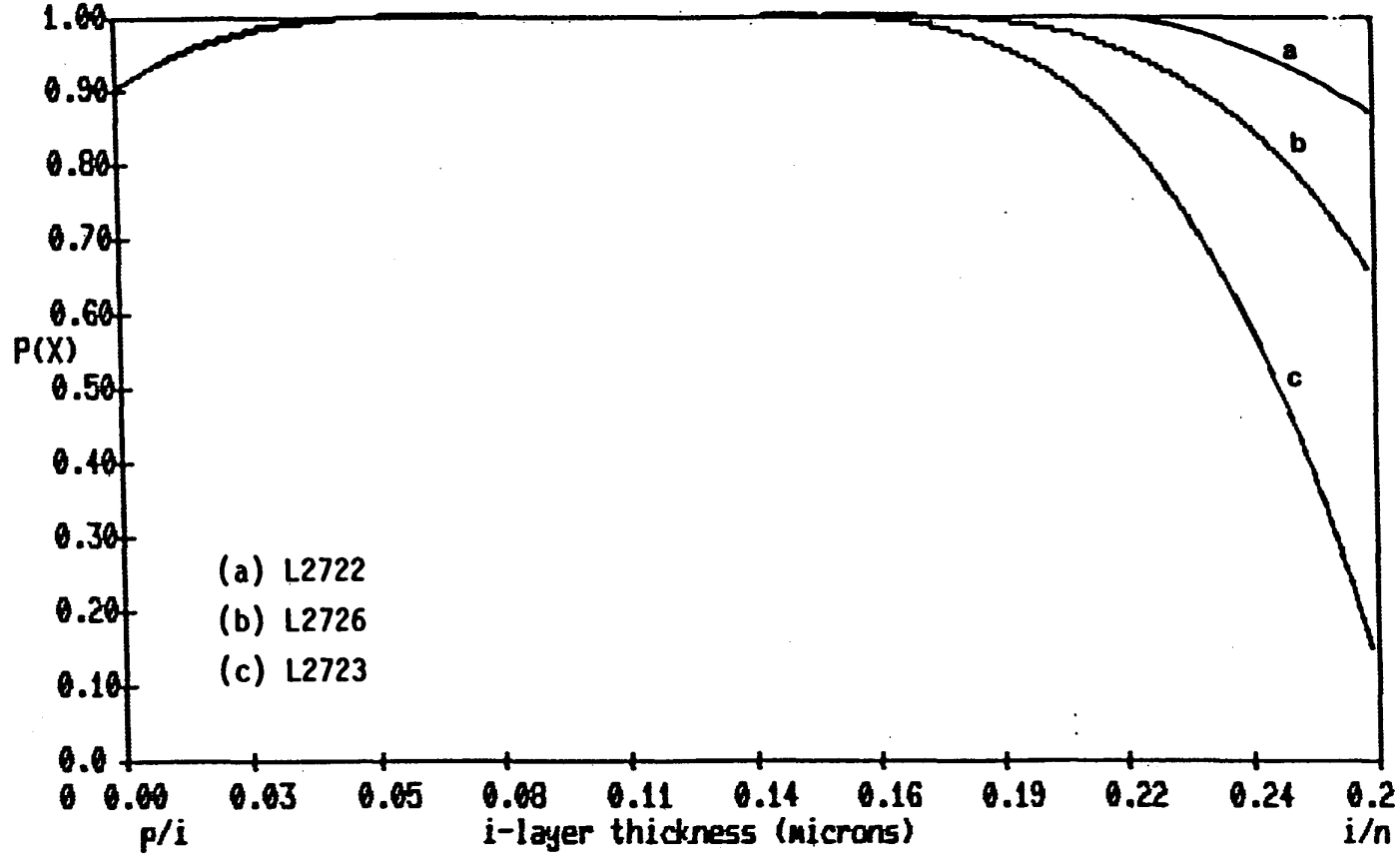

Fig. 23. Internal collection efficiency versus i-layer thickness for three a-Si alloy devices with varying amounts of band-gap profiling in their intrinsic layers (see Fig. 19 for the band-gap profiles).

case at the n^+i interface. We can see that the i-layer grading of sample L2722 very much aids hole transport over that of the constant band-gap sample L2726. If, however, the grading is reversed as in sample L2723, we see a very sharp decrease in the hole transport properties.

In addition to aiding hole transport with these graded structures, optical absorption profiles reveal that the mean carrier path length can be increased or decreased by this optical band-gap grading. For sample L2722, not only does the affinity grading aid hole transport over that of the constant band-gap case of sample L2726 (recall Fig. 23), but the mean hole path length is decreased significantly by skewing the absorption profile toward the p^+ layer. This is a result of the narrower band-gap material being near the p^+i interface. The reverse situation occurs in sample L2723; that is, the absorption is pushed toward the back of the device due to the narrower band-gap material being near the n^+ layer, thus increasing the mean path length for holes.

4.5. DEVICE STATUS

Employing the novel graded i-layer structure discussed above, we have improved the performance of amorphous silicon-germanium alloys and devices. The improvement in the narrow band-gap alloy resulted in better fill factor and higher open-circuit voltage for a given short-circuit current density. This has allowed us to incorporate more germanium into the alloy and further increase the spectrum-splitting feature of multi-junction devices. The following paragraphs summarize our present device status.

Top Cell

The top cell in a triple configuration is exposed to the full solar insolation. It is very important that the top cell has high voltage and good fill factor. The current density depends on the matching of various multi-junction device configurations. Figure 24 shows the J-V characteristic of a top cell with approximately 8 mA/cm^2. This device exhibits both high open-circuit voltage and fill factor.

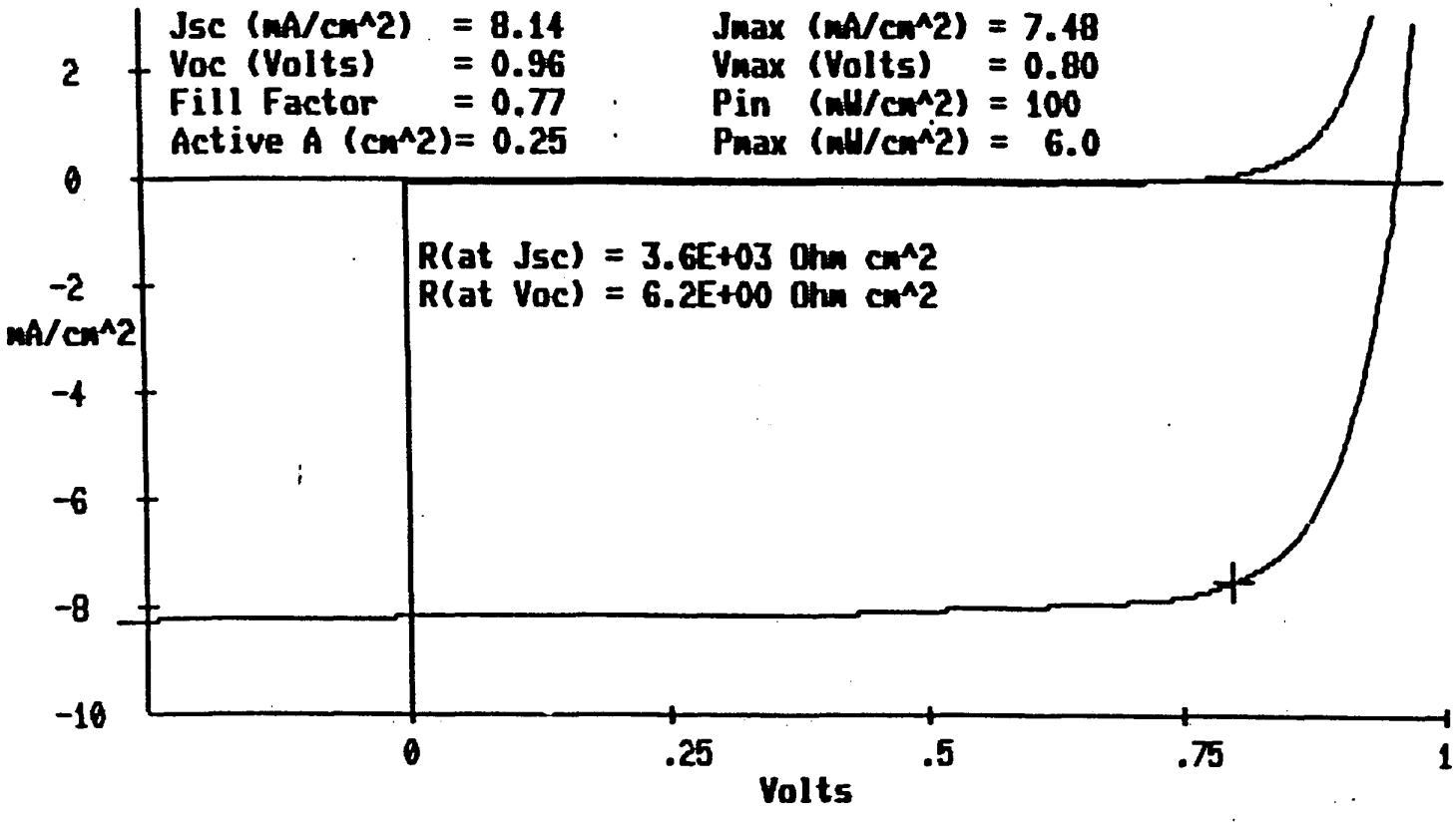

Fig. 24. J-V characteristic of a thin amorphous silicon device measured under global AM1.5 illumination at 25°C.

Bottom Cell

As was mentioned earlier, we have incorporated a novel structure in the amorphous-silicon germanium cell which resulted in an improved performance suitable for the bottom of a tandem or triple device. The highest current density observed is approximately 23 mA/cm^2. Figure 25 shows the J-V characteristic of a device that has Jsc = 22.4 mA/cm^2, Voc = .71 volt, FF = .58, and 9.2% efficiency measured under global AM1.5. The quantum efficiency curve of this device is shown in Fig. 26. It is noted that the collection is 46% at 800 nm, 29% at 850 nm and 8% at 900 nm.

Tandem Devices

Using the cell shown in Fig. 25 as the bottom cell and standard amorphous silicon alloy in the top cell, we have fabricated tandem devices and achieved a 13% efficiency. Figure 27 shows the J-V characteristic of this device which exhibits Jsc = 11.9 mA/cm^2, Voc = 1.635 volts, and FF = 0.67. Figure 28 displays the quantum efficiency curve of this device. It is noted that the total photocurrent generated from this tandem structure is 24 mA/cm^2, a significant result.

Triple Devices

The best triple device made to date is a 13.7% device using amorphous silicon-germanium alloy in the bottom cell and amorphous silicon alloy in the top and the middle cells. The J-V characteristic and quantum efficiency curves are shown in Figs. 29 and 30, respectively. Since we have been successful in incorporating more germanium into the narrow band-gap material, we can reoptimize the middle cell by incorporating a small amount of germanium into it. We anticipate a higher short-circuit current density from this new structure.

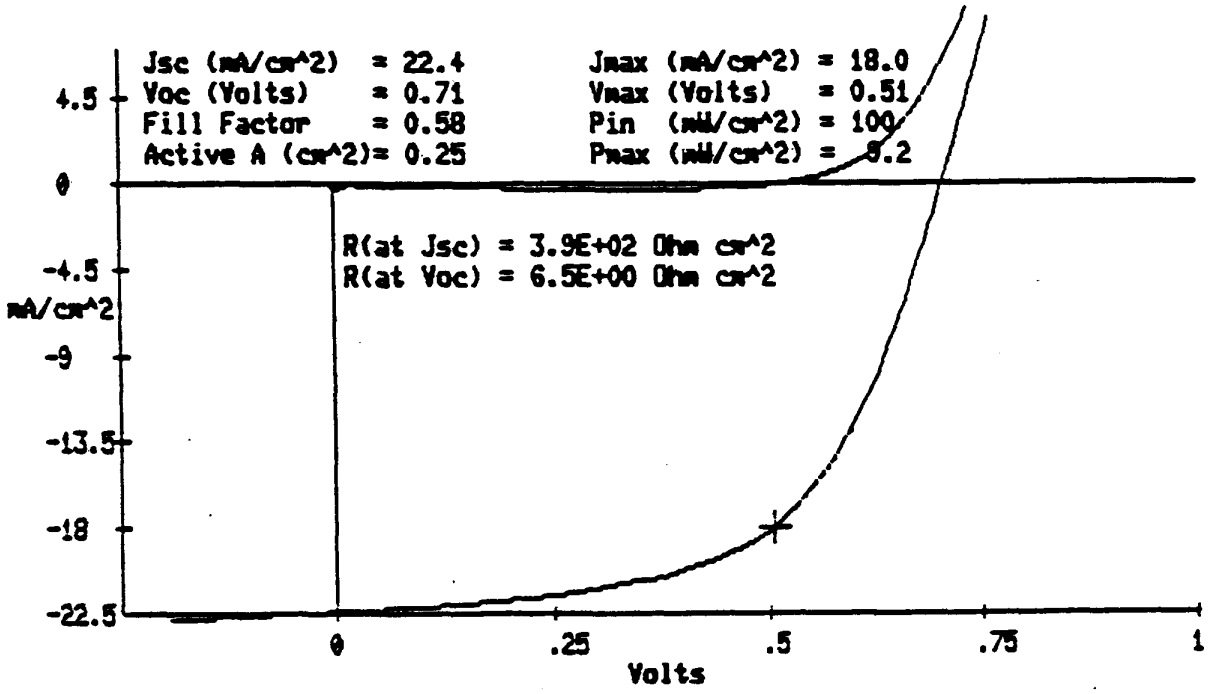

Fig. 25. J-V characteristic of a narrow band-gap amorphous silicon-germanium device measured under global AM1.5 illumination at 25°C.

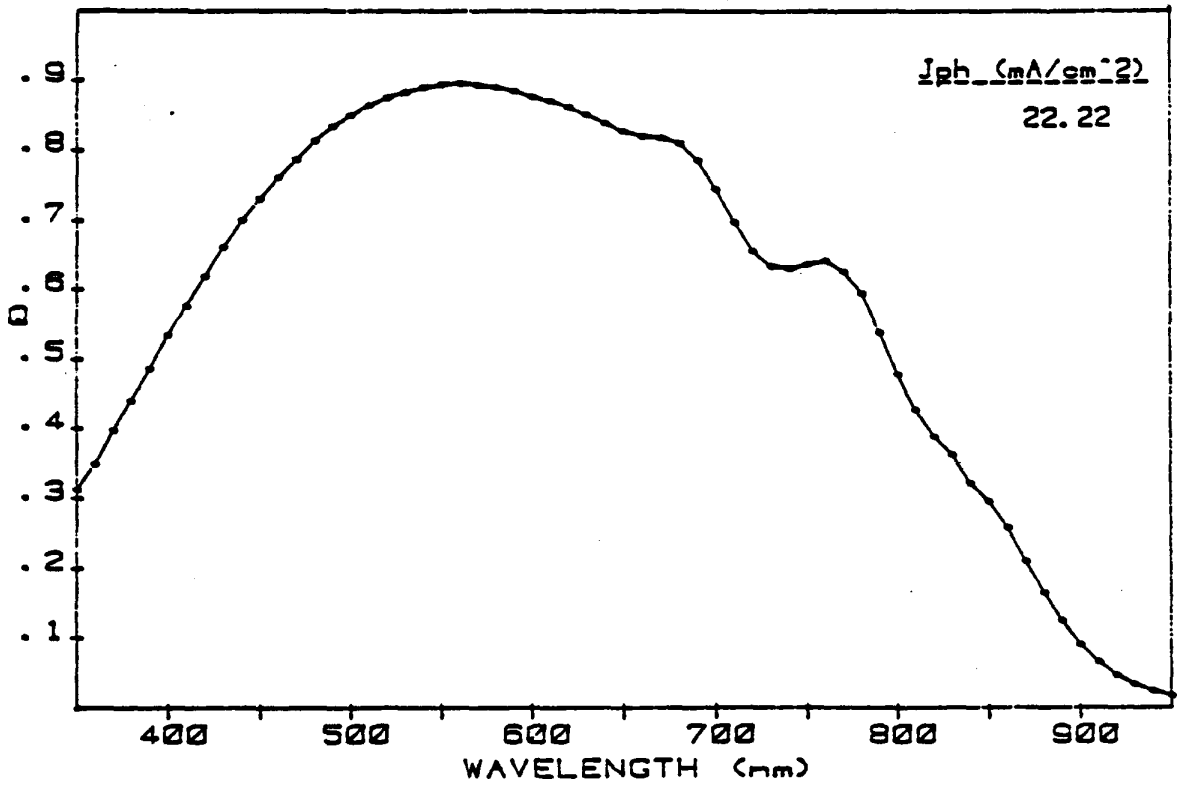

Fig. 26. Quantum efficiency of the single-junction device shown in Fig. 25.

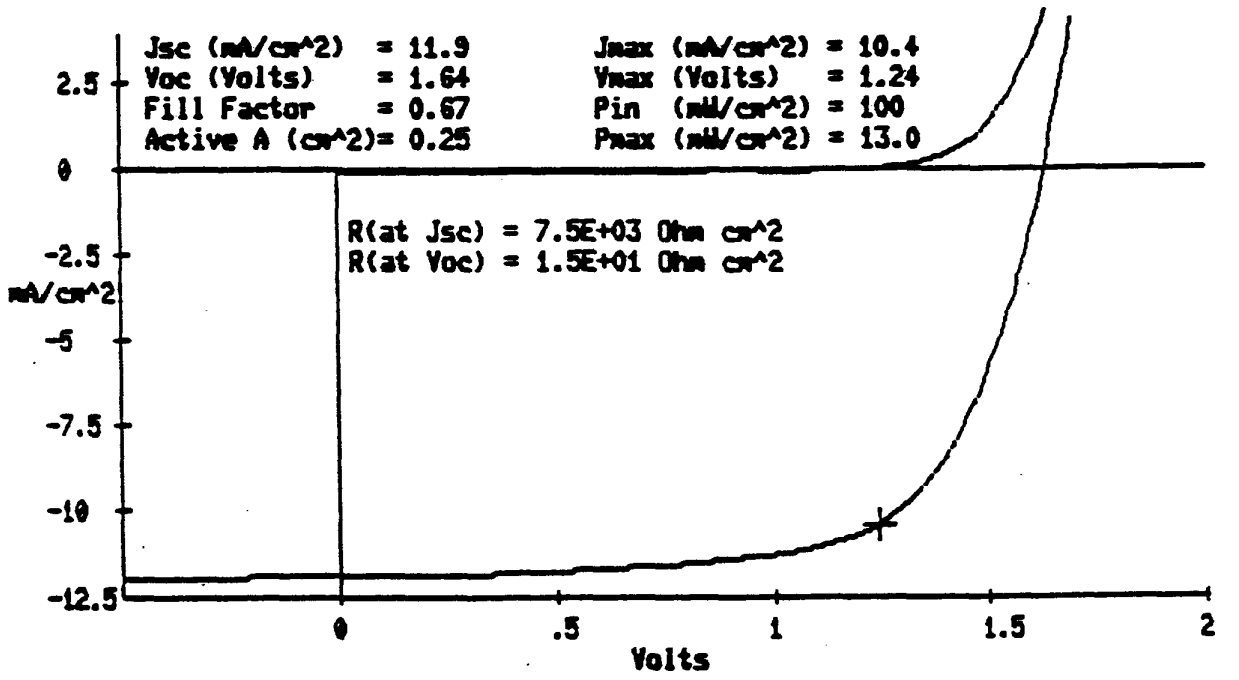

Fig. 27. J-V characteristic of a two-cell tandem device measured under global AM1.5 illumination at 25°C using a dual-source simulator.

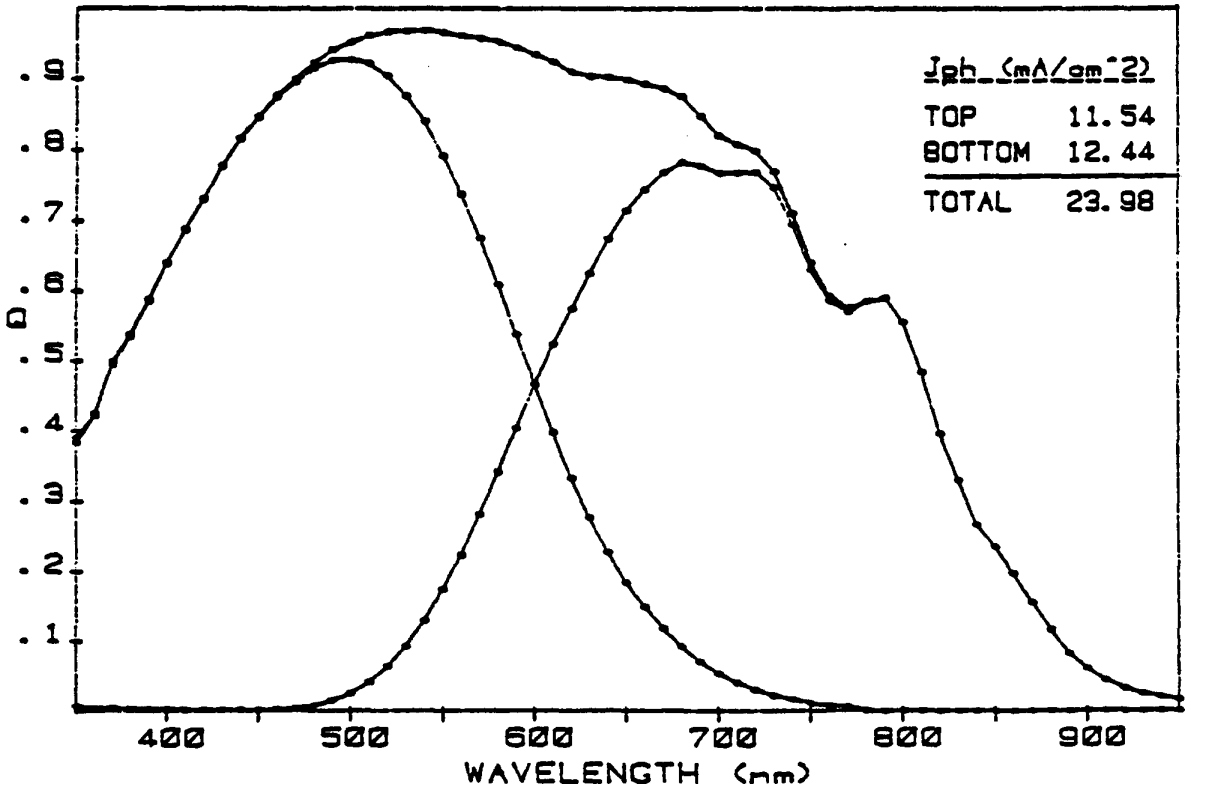

Fig. 28. Quantum efficiency of the tandem device shown in Fig. 27.

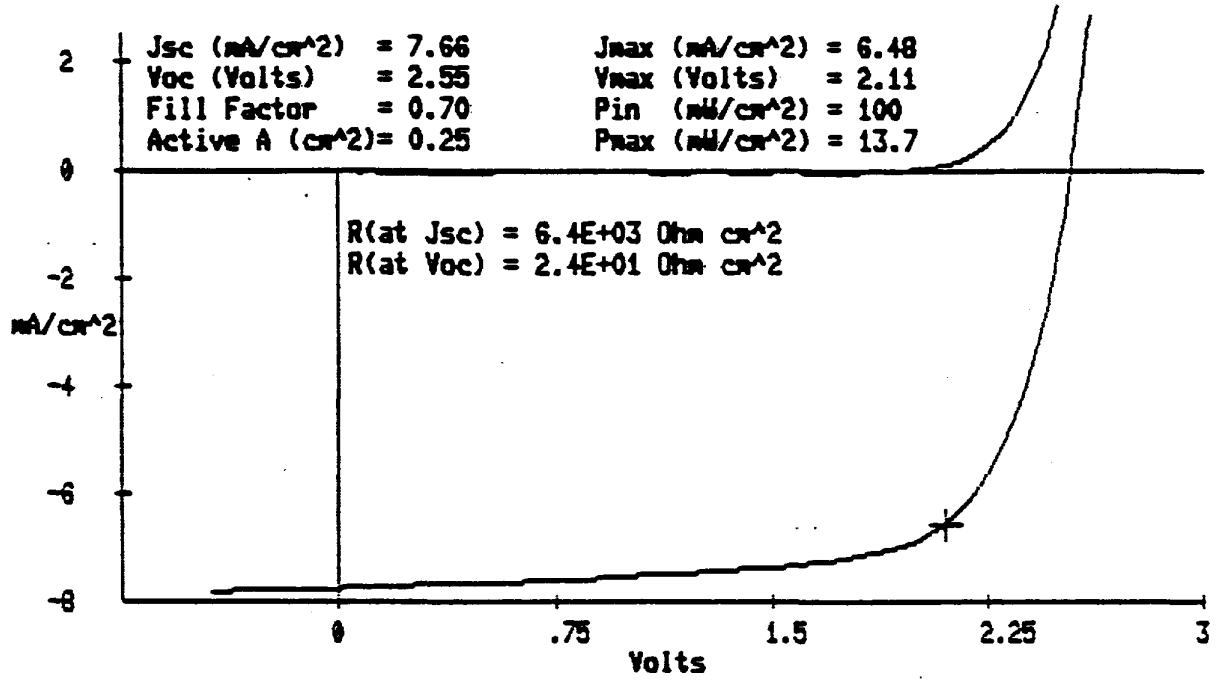

Fig. 29. J-V characteristic of a three-cell triple device measured under global AM1.5 illumination at 25°C using a triple-source simulator.

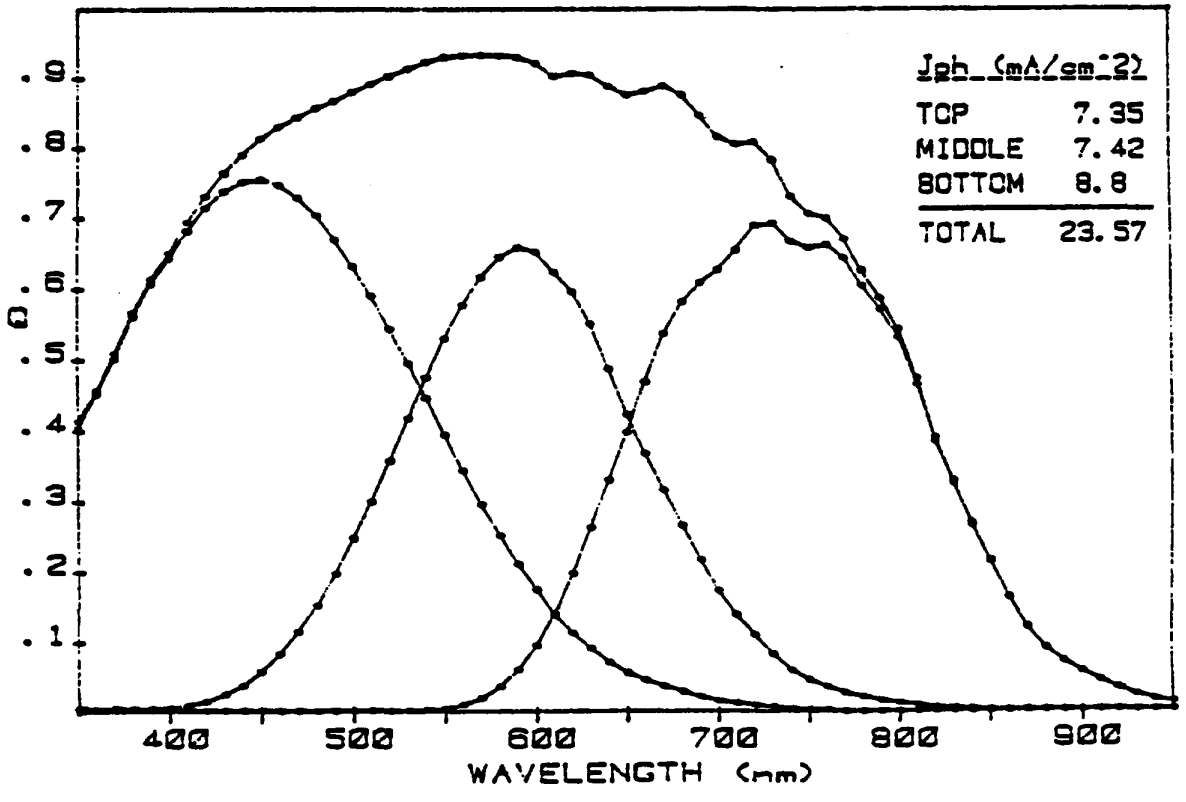

Fig. 30. Quantum efficiency of the triple device shown in Fig. 29.

4.6. EFFECT OF PH_3 CONCENTRATION IN THE n^+ LAYER ON SINGLE AND TANDEM DEVICE PERFORMANCE

We have studied the performance of devices with various PH_3 concentrations in the n^+ layer. The intrinsic layer of these devices has a thickness of approximately 1000Å, and the devices were deposited onto stainless steel substrates. Figure 31 shows the AM1.5 global J-V characteristics of four devices with different PH_3 concentrations. Figure 32 shows the blue and red responses for those devices shown in Fig. 31. It can be seen that the blue fill factor is about the same for all four cases, while the red response becomes poorer as the PH_3 concentration increases (from a to d) in the n^+ layer. It is easy to understand that residual phosphorous in the intrinsic layer makes the material ν-type and hinders the hole transport properties. One would then incline to use the lowest possible PH_3 concentration in the n^+ layer of the top cell in tandem devices.

Along these lines, we have made four tandem devices using the four cases in Fig. 31 as the top cell and the standard amorphous silicon device with a 5000Å thick intrinsic layer as the bottom cell. Figure 33 shows the J-V characteristics for these four tandem devices. An obvious kink is observed in the lowest PH_3 case (curve a), while the highest PH_3 concentration in the n2 layer (curve d) gives rise to higher voltage and better fill factor. The higher voltage is interpreted as due to the sharper p/i junction in the top cell associated with ν-type intrinsic material, while the higher fill factor is the result of a better contact between p1 and heavily doped n2 layers, as evidenced from the reduced series resistance of the device. Based on these results, therefore, one must be careful when applying results from single-junction device studies to the multi-junction case. As seen from the above example, the single-junction result behaves quite differently when it is applied to a tandem device.

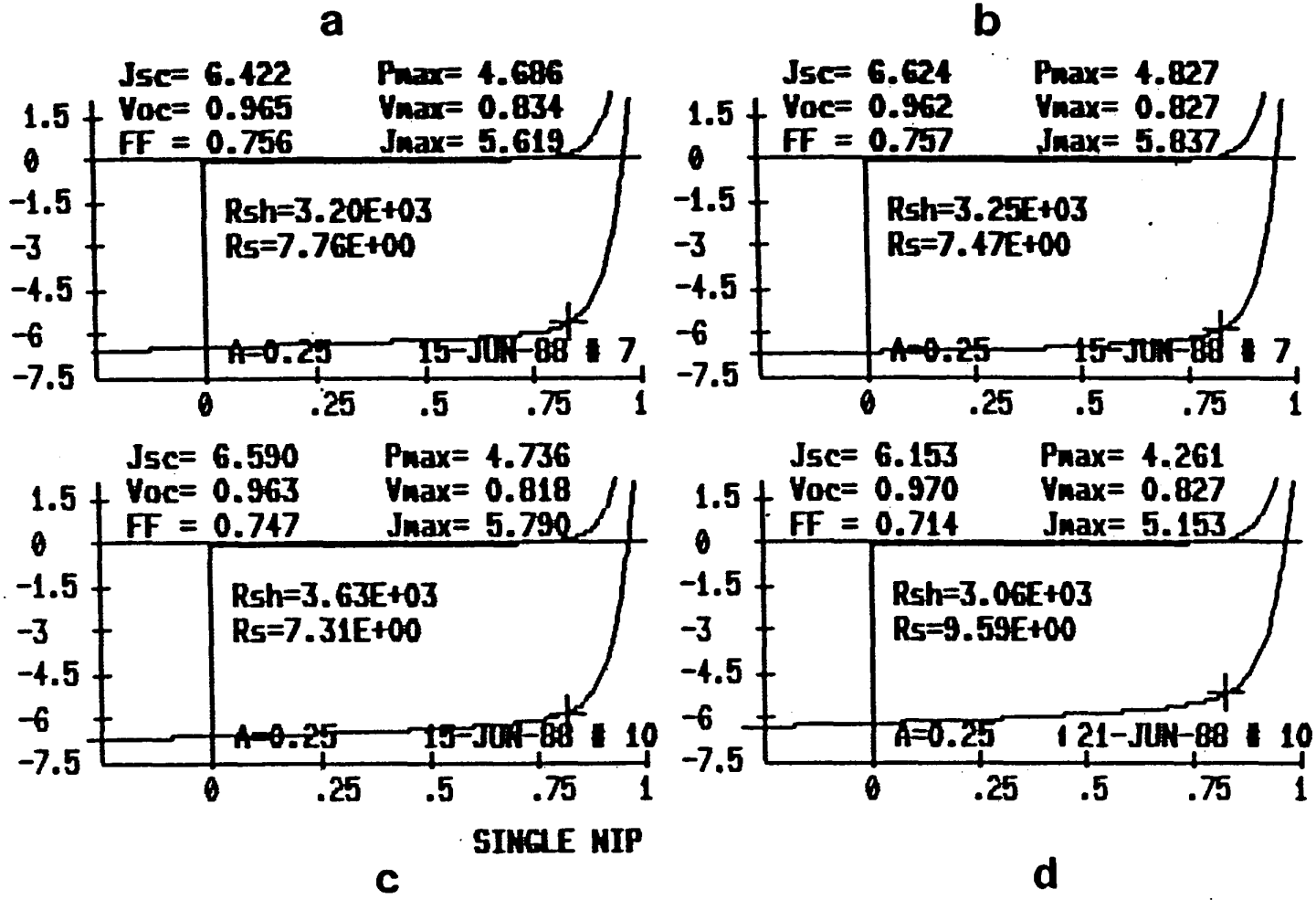

Fig. 31. J-V characteristics under AM1.5 illumination for four single-junction a-Si alloy devices with varying amounts of PH_3 in their n^+ layers, increasing in concentration from a to d.

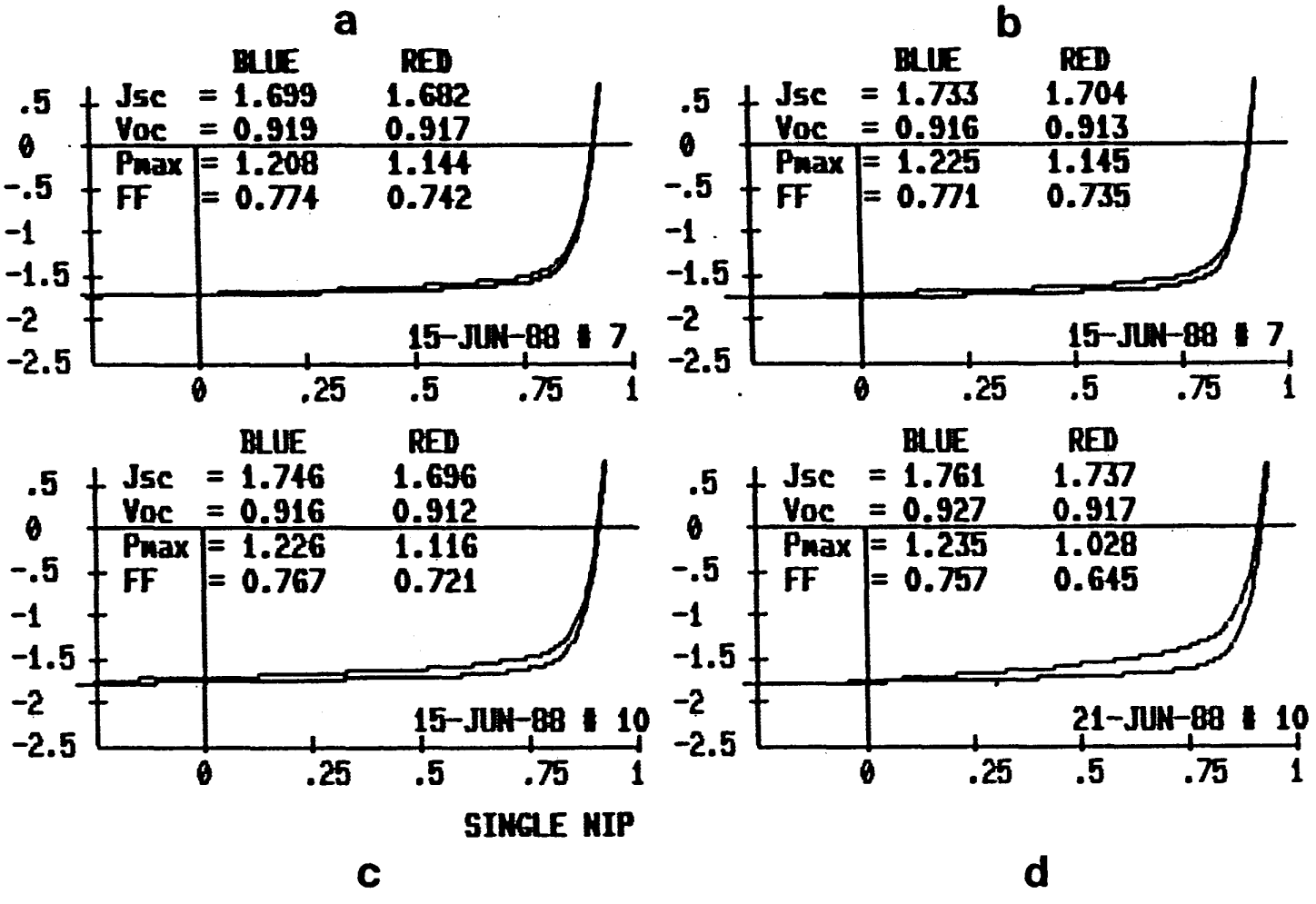

Fig. 32. J-V characteristics under blue- and red-light illumination for four single-junction a-Si alloy devices with varying amounts of PH_3 in their n^+ layers, increasing in concentration from a to d.

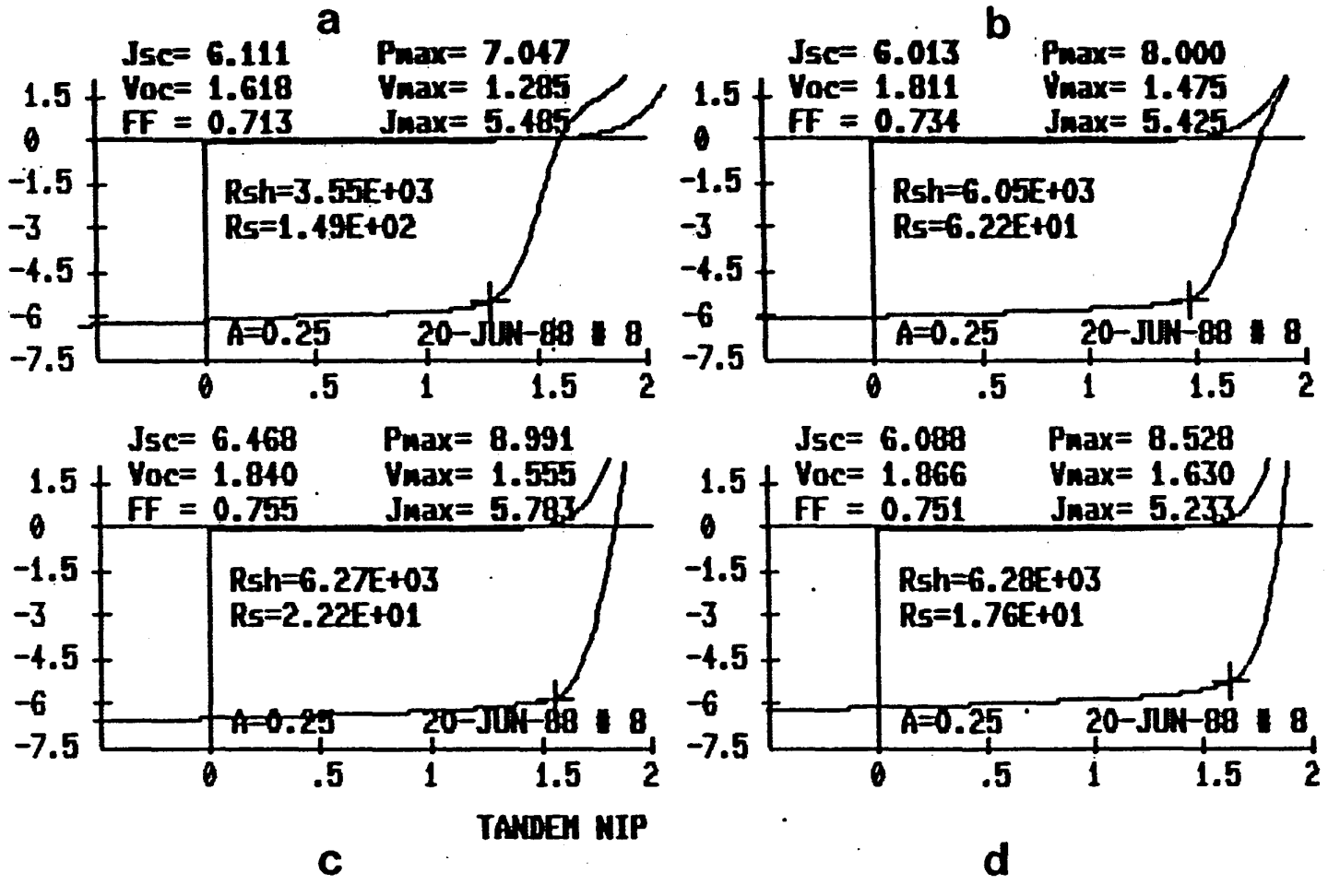

Fig. 33. J-V characteristics under AM1.5 illumination for four two-cell tandem a-Si alloy devices with varying amounts of PH_3 in their $n2^+$ layers, increasing in concentration from a to d.

4.7. DEVICE STABILITY STUDIES

Figure 34 shows the stability result for a high-efficiency triple-junction device under AM1.5 illumination. This device showed a typical degradation after 240 hours of about 13%. This device had an initial efficiency of over 13% evaluated under a triple-source simulator set for AM1.5 global standard test conditions. This figure also shows the stability of the other J-V parameters: FF, Voc, and Jsc.

Figure 35 shows the degradation of two single-junction devices with graded band-gap intrinsic layers versus hours of red-light illumination. We see that the device with the higher efficiency also degrades less. This can be understood since the affinity grading which aids hole transport (narrow band-gap near the p^+ layer) also minimizes recombination -- the major cause of Staebler-Wronski degradation - resulting in better carrier collection and a more stable device, in addition to its higher conversion efficiency.

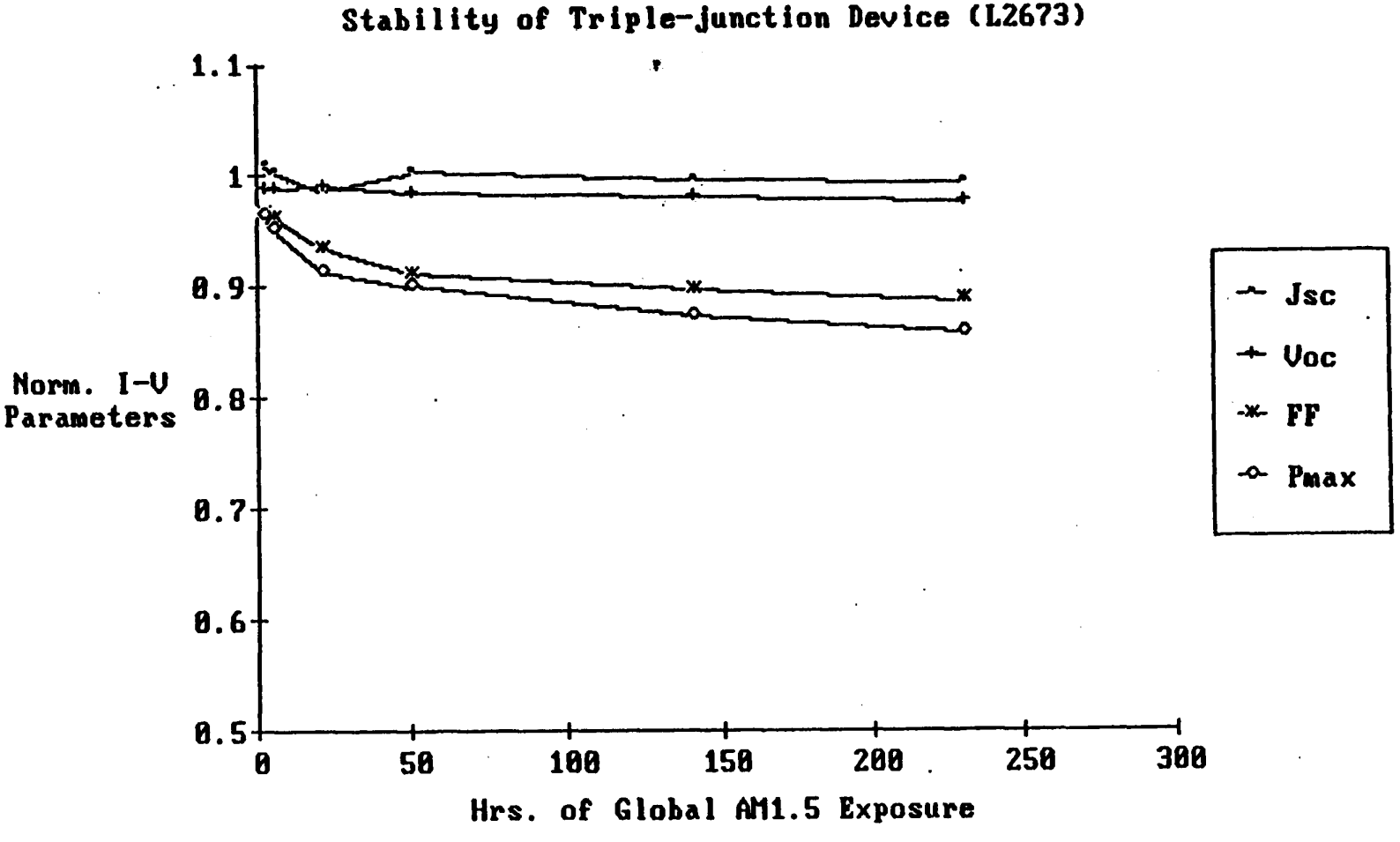

Fig. 34. Stability of a triple-junction a-Si/a-Si/a-Si:Ge alloy solar cell, showing the four I-V parameters versus exposure time under 1-sun illumination. The device had an initial efficiency of over 13% as measured under a triple-source simulator set to AM1.5 global standard test conditions.

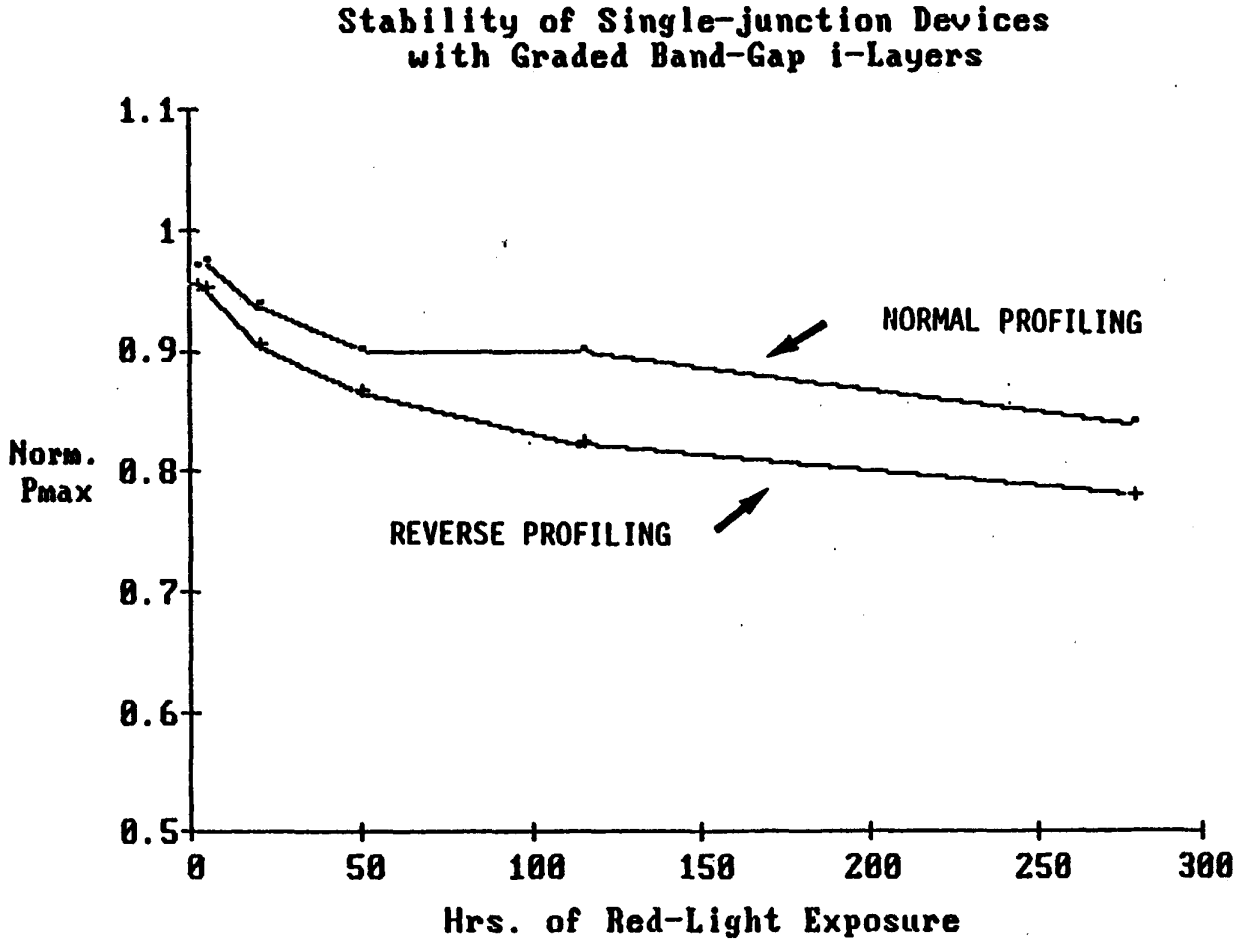

Fig. 35. Stability of two single-junction a-Si:Ge alloy solar cells with graded band-gap intrinsic layers, showing Pmax versus exposure time under red-light illumination. The i-layers of these devices were graded in opposite directions with their band-gap profiles as shown in Fig. 19.

REFERENCES

1. R.R. Arya, A. Catalano and P.S Oswald, Appl. Phys. Lett. 49, 1089, 1986.
2. S. Yamanaka, S. Kawamura, M. Konagi and K. Takahashi, Tech. Digest of the Intl. PVSEC-3, Tokyo, Japan, 1987, p. 709.
3. A. Pawlikiewicz and S. Guha, MRS Symposium Proc. 118, 599, Reno, Nevada (1988).
4. M. Hack and M. Shur, J. Appl. Phys. 58(2), 997 (1985).
5. A. Pawlikiewicz and S. Guha, Proc. 20th IEEE PVSC, Las Vegas, Nevada, 1988.
6. J.S. Payson and S. Guha, Phys. Rev. B, 32(2), 1326 (1985).
7. A. Madan and M.P. Shaw, The Physics and Application of Amorphous Semiconductors, Acad. Press, p. 51 (1988).
8. C.R. Wronski, B. Abeles, T. Tiedje, C.D. Cody, Solid State Commun., 44, 1423 (1982).
9. R.A. Street, J. Zesch, J. Thompson, Appl. Phys. Lett. 43, 672 (1983).
10. M. Hack, S. Guha, M. Shur, Phys. Rev. B, 30, 6991 (1984).
11. A. Pawlikiewicz, work performed for SERI under Contract No. ZB-7-06003-4, to be published.
12. G.W. Taylor and J.G. Simmons, J. Non-Cryst. Solids, 8-10, p. 940 (1972).
13. A. Madan and M.P. Shaw, The Physics and Application of Amorphous Semiconductors, Acad. Press, p. 64 (1988).
14. T. Takahama et al., Japanese Journal of Applied Physics, Vol. 25, #10, Oct. 1986, pp. 1538-1541.

Document Control Page	1. SERI Report No. SERI/STR-211-3526	2. NTIS Accession No. DE89009444	3. Recipient's Accession No.

4. Title and Subtitle

Research on High-Efficiency, Multiple-Gap, Multijunction Amorphous-Silicon-Based Alloy Thin-Film Solar Cells, Semiannual Subcontract Report, 1 Mar. 1988-31 Aug. 1988

5. Publication Date
June 1989

6.

7. Author(s)
S. Guha, Principal Investigator

8. Performing Organization Rept. No.

9. Performing Organization Name and Address

Energy Conversion Devices, Inc.
Troy, Michigan 48084

10. Project/Task/Work Unit No.

11. Contract (C) or Grant (G) No.
(C)ZB-7-06003-4
(G)

12. Sponsoring Organization Name and Address

Solar Energy Research Institute
1617 Cole Boulevard
Golden, Colorado 80401-3393

13. Type of Report & Period Covered
Technical Report

14.

15. Supplementary Notes
SERI Technical Monitor: Byron Stafford, (303) 231-7126

16. Abstract (Limit: 200 words)

This report presents results of research on advancing our understanding of amorphous-silicon-based alloys and their use in small-area multijunction solar cells. The principal objectives of the program are to develop a broad scientific base for the chemical, structural, optical, and electronic properties of amorphous-silicon-based alloys; to determine the optimum properties of these alloy materials as they relate to high-efficiency cells; to determine the optimum device configuration for multijunction cells; and to demonstrate proof-of-concept, multijunction, a-Si-alloy-based solar cells with 18% efficiency under standard AM1.5 global insolation conditions and with an area of at least 1 cm^2. A major focus of the work done during this reporting period was the optimization of a novel, multiple-graded structure that enhances cell efficiency through band-gap profiling. The principles of the operation of devices incorporating such a structure, computer simulations of those, and experimental results for both single- and multijunction cells prepared by using the novel structure are discussed in detail.

17. Document Analysis

a. Descriptors Photovoltaic cells ; silicon solar cells ; amorphous state ; graded band gaps ; thin films

b. Identifiers/Open-Ended Terms

c. UC Categories
271

18. Availability Statement

National Technical Information Service
U.S. Department of Commerce
5285 Port Royal Road
Springfield, Virginia 22161

19. No. of Pages
70

20. Price
A04